TÉCNICO LISBOA

WC-Cu cermet materials: production and characterization

Flávio Diogo Gonçalves Guerreiro

Thesis to obtain the Master of Science Degree in

Materials Engineering

Supervisors: Prof. Eduardo Jorge da Costa Alves
PhD Marta Sofia Rosado Silva Dias
Co-Supervisor: Eng. Carlos Miguel Coelho

Examination Committee

Chairperson: Prof. Maria de Fátima Reis Vaz
Supervisor: PhD Marta Sofia Rosado Silva Dias
Member of the Committee: Prof. Alberto Eduardo Morão Cabral Ferro

November 2015

This page was intentionally left blank

Acknowledgments

Firstly, I would like to express my sincere gratitude to my advisors Doctor Eduardo Alves and Doctor Marta Dias for the continuous support of my MSc study, for their patience, motivation, and knowledge. Their guidance helped me in all the time of research and writing of this thesis.

Besides my advisors, I would like to acknowledge DIAPOR – Diamantes de Portugal, in particular to the Engineers Miguel Coelho and João Teixeira for providing the resources needed to accomplish this work.

I am also thankful to Doctor Umesh Vinaica from IST for thermal diffusivity measurements. Without his precious support it would not be possible to conduct this research.

I wish to thank to Doctor Patrícia Carvalho and IPFN for have given me the opportunity to be part of a great institution.

I would like to express my deeply gratitude to all my friends for the friendship and for helping me to have great times.

Last but not the least, I would like to thank my family: my parents and to my brother for their love and support through the years and for making available resources for doing this work. Without them my education and growth as a person and professional would not be possible.

Resumo

Devido às semelhanças entre o tungsténio e carboneto de tungsténio desenvolveram-se cermets WC-Cu com diferentes frações volúmicas de cobre (25, 50 e 75%) com o intuito destes materiais atuarem como barreiras térmicas. Os materiais foram produzidos por prensagem a quente a temperaturas que variam entre os 900 e os 1100 ºC e pressões entre os 22 e 47 MPa. A caracterização microestrutural dos cermets foi feita por microscopia electrónica de varrimento associada a espectroscopia de raios-X por dispersão de energia. A difusividade térmica foi medida pela técnica de laser flash. A micro-dureza e densidade relativa foram também determinadas. Os materiais consolidados apresentam uma dispersão homogénea de WC na matriz de cobre sem a formação de óxidos e com densidades que variam entre os 91 e 95%. Não se observou a decoesão entre as partículas e a matriz nas zonas indentadas. A difusividade térmica dos materiais é inferior à difusividade do cobre e do tungsténio, o que sugere que estes materiais possam de facto atuar como barreiras térmicas.

Abstract

Due to the similar properties between tungsten and tungsten carbide as well as to the extensive body on knowledge on WC cermets, WC-Cu cermets with 25, 50 and 75 % volume fraction of copper have been devised for thermal barriers. The composite materials have been prepared by hot pressing at temperatures ranging from 900 to 1100 ºC with pressures of 22 to 47 MPa. These novel cermets were investigated by scanning electron microscopy coupled with energy dispersive X-ray spectroscopy. The thermal conductivity was measured by laser flash technique and the microhardness and geometric density were also evaluated. The consolidated materials consisted of homogeneous dispersion of WC particles in the Cu matrix without any evidence for oxide formation and with densifications of about 91-95%. No interfacial decohesion was detected in indented regions. The cermets thermal diffusivity is lower compared to copper or tungsten, as desirable for thermal barrier materials.

Keywords: WC-Cu cermet, hot pressing, thermal diffusivity, densification.

Index

List of Figures

List of Tables

Abbreviations

BSE	Backscattered electrons
CTE	Coefficient of thermal expansion
DBTT	Ductile to brittle transition temperature
DEMO	Demonstration fusion power plant
EDS	Energy dispersive X-ray spectroscopy
FGM	Functionally graded materials
HIP	Hot isostatic pressing
HP	Hot pressing
HV	Vickers hardness
IR	Infrared
ISO	International Organization for Standardization
ITER	International thermonuclear experimental reactor
OPS	Silica oxide polishing suspension
SE	Secondary electrons
SEM	Scanning electron microscopy

List of Symbols

A	Area of indentation
C_0	Constant determined by the initial conditions
C_D	Diamond
C_n	Constant determined by the initial conditions
cos	Cosine function
C_p	Specific heat
D	Diameter of a cylindrical section of the specimen
d	Mean of the diagonals of the indentation
E_0	Energy of the primary electron beam
E_1	Young's modulus of CuCrZr
E_2	Young's modulus of W
F	Load applied
$f(x)$	Function describing the temperature distribution
f_{WC}	Volume fraction of tungsten carbide
g	Thickness of a thin surface layer
$g(r,t)$	Internal sources and sinks of heat
H	Height of a cylindrical section of the specimen
K_y	Constant corresponding to an y percent rise in the rear face temperature

L	Thickness of the sample
Q	Energy pulse of the laser
sin	Sine function
T	Temperature
t	Time
T_0	Reference temperature
$t_{0.5}$	Time required to the rear face temperature reach 50% of its maximum temperature
t_1	Wall thickness of CuCrZr
$T_{1,average}$	Average temperature of CuCrZr
t_2	Wall thickness of W
$T_{2,average}$	Average temperature of W
t_y	Time required to the temperature reach y of the maximum temperature
$V(L,t)$	Percent rise in the rear face temperature of the disk
W_f	W-monofilament
x	Position in the thickness direction of the sample
α	Thermal diffusivity
α_1	Coefficient of thermal expansion of CuCrZr
α_2	Coefficient of thermal expansion of W
λ	Thermal conductivity
π	Pi constant
ρ	Density
ρ_{cermet}	Density of the cermet
ρ_{cu}	Density of copper
ρ_{WC}	Density of tungsten carbide
$\sigma_{0.2}$	Standard deviation associated to the HV0.2 measurements
σ_2	Standard deviation associated to the HV2 measurements
$\sigma_{mismatch}$	Mismatch stress caused by the difference in coefficient of thermal expansion between W and CuCrZr.
υ_1	Poisson's ratio of CuCrZr
υ_2	Poisson's ratio of W
$\frac{\partial^2 T}{\partial x^2}$	Second-order derivative of temperature at position x
$\frac{\partial T}{\partial t}$	Rate of change in temperature
∇^2	Laplace operator
$\frac{dT}{dx}$	First-order derivative of temperature in order of position x
∇T	Gradient of Temperature
$\nabla \lambda$	Gradient of thermal conductivity

1 Introduction

This chapter tries to make an overview of what is the International thermonuclear experimental reactor and the problems related to the high heat flux materials. The reader will be introduced to the problems generated at the cooling pipe - tungsten interface due to the different operation temperatures as well to the solutions proposed to solve those problems. Later on this chapter the concept of cermet materials is explained and described some of their properties.

1.1 Background

The International thermonuclear Experimental Reactor (ITER) is a nuclear fusion reactor based on the tokamak concept of magnetic confinement [1]. This type of device plasma is confined in the shape of a torus due to the interaction between a magnetic field and the plasma particles. Seven components of the ITER can be identified: magnets; vacuum vessel; blanket; divertor; diagnostics; external eating and cryostat.

The magnet system of ITER includes 18 superconducting toroidal field and 6 poloidal field coils, a central solenoid, and a set of correction coils that magnetically confine, shape and control the plasma inside the vacuum vessel. The poloidal and toroidal field coils lie between the vacuum vessel and the cryostat. The toroidal field magnets surrounding the torus produce a magnetic field that travels around the torus in circles, whose primary function is to confine the plasma particles. The poloidal field magnets pinch the plasma away from the walls and contribute in this way to maintaining the plasma's shape and stability. The poloidal field is induced both by the magnets and by the current drive in the plasma itself. In addition a central solenoid, acting like a large transformer contributes to the shaping of the field lines in the divertor region and to vertical stability control. Covering the vacuum vessel and the superconducting magnets is the cryostat, a stainless steel structure that provides a vacuum environment. It consists on two concentric walls connected by horizontal and vertical ribs. Helium gas acting as thermal barrier fills the space between the two walls. Due to the difference in temperature of the vacuum vessel and the cryostat large bellows connect these structures to allow thermal contraction and expansion in the structures.

The vacuum vessel is the first safety containment barrier inside the cryostat where the fusion reaction takes place. The plasma particles spin around continuously in its torus shape and the volume of fusion plasma is defined by the size of the vacuum vessel itself. To provide shield from the heat and neutron fluxes of the fusion reaction the vacuum vessel is covered by a wall called the blanket. This wall is modular and consists of 440 individual segments, each measuring 1 x 1.5 m. In the blanket the neutrons are slowed down and their kinetic energy is transformed into heat energy and collected by the coolants. Each segment has a detachable first wall made in beryllium and a semi-permanent blanket shield made of high-strength copper and stainless steel. Together with the divertor they are the components that face the plasma. The divertor consists on 54 remotely removable cassettes located along the bottom of the vacuum vessel. Each cassette holds 3 plasma-facing components (targets): the inner and outer vertical targets and the dome. The cassette of the divertor is made of stainless steel and supports the vertical targets and the dome as shown in Figure 1.1. The targets

have the function of accommodating the heat flux during operation and providing the required lifetime under the operating conditions of the reactor. The main function of the dome is to retain recycling neutrals inside the divertor region. Small tungsten (W) armour covers the targets and dome - monoblocks.

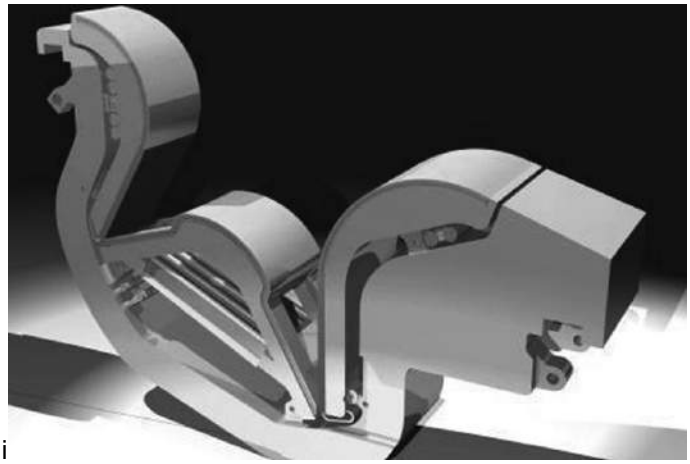

i

Figure 1.1: Cassette of the divertor of ITER [2]**.**

The design and technological features of the components described above are essential to ensure the best performance of the ITER. The nuclear fusion reaction between two hydrogen isotopes (deuterium and tritium) produces helium, a neutron and energy. However, for the reaction to take place temperatures in the order of 150 millions degrees are required. To achieve such temperatures the ITER tokamak will be supported by 3 external heating sources. The helium particles carry electric charge that will respond to the magnetic field inside the reactor and remain within it. Nevertheless, a great amount of the energy produced in the reaction is carried away from the plasma by the neutrons that are unaffected by the magnetic field since they have no electrical charge. The surrounding walls of the tokomak will absorb these neutrons. At the divertor the energy carried by the neutrons will be transferred as heat through the walls, subsequently the heat will be used to produce steam and electricity.

The demonstration fusion power plant (DEMO) with technology based on realistic extrapolation from ITER will use water as the baseline divertor coolant as it can achieve high heat transfer rates.

1.2 Motivation

Tungsten was chosen as a plasma facing material due to its high sputtering threshold, high melting point, high tensile strength and great corrosion resistance [3]. However, a major disadvantage of current tungsten-grades is their relatively high ductile-to-brittle transition temperature [4]. A CuCrZr alloy has been selected as heat sink material to remove heat from the plasma facing components due to its high conductivity, strength and microstructural stability [5]. This alloy suffers embrittlement under irradiation, however among Cu alloys it shows better mechanical properties (strength and fracture toughness) and has more operational margin as the divertor heat sink material. Joining these two different materials (W and CuCrZr) and ensure that they operate without failure revealed to be a challenge due to the stresses caused by the W/CuCrZr joint. Three main sources of stresses affecting the pipe material can be identified: (i) the internal pressure of the water coolant; (ii) the temperature gradient due to the heat flux and (iii) the difference in the thermal expansion between the tube and the surrounding tungsten. The mismatch in the coefficient of thermal expansion (CTE) between W and CuCrZr alloy and the difference in Young's modulus cause high residual and thermal stresses at the W / CuCrZr interface when exposed to the high-heat loads. Thermal stresses may cause cracking, delamination and reduce the lifetime of the components by detachment. The mismatch stress caused by the difference in CTE between W and CuCrZr can be expressed as [6]:

$$\sigma_{mismatch} = \frac{\alpha_2\left(T_{2,average} - T_0\right) - \alpha_1(T_{1,average} - T_0)}{\frac{(1-\upsilon_2)t_1}{t_2 E_2} + \frac{1-\upsilon_1}{E_1}} \tag{1.1}$$

Where α, t, T, υ and E correspond to CTE, wall thickness, temperature, Poisson's ratio and Young's modulus, respectively. T_0 is a reference temperature equal to 22 ºC. If the subscripts 1 and 2 designate the CuCrZr and W, respectively, one can see that the mismatch stress is reduced if T_2 is increased and T_1 is reduced.

In addition to the mismatch stress there is the problem to ensure that the temperatures of both W and CuCrZr are under their operation window temperature. The W surface limiting temperature is associated with the re-crystallization of W, which occurs at 1300 ºC. When heated above the recrystallization temperature, the structure of tungsten is altered due to grain growth causing an increase in ductile to brittle transition temperature (DBTT) and reducing other mechanical properties as strength and hardness [7]. Relatively to the copper alloy the operating temperature must be kept above 200 ºC because it looses ductility under irradiation at temperatures below 180 ºC [8]. Moreover the service temperature of this material is relatively low and, therefore, operation at higher temperatures demands thermal barriers between the plasma-facing W and the CuCrZr heat sink, which is illustrated in Figure 1.2. The purpose of the interlayer is to reduce the conductance of heat assuring that both W and CuCrZr operate within their recommended temperature windows. If the interlayer is very compliant it must accommodate the difference in the CTE of both W and CuCrZr reducing the mismatch stress.

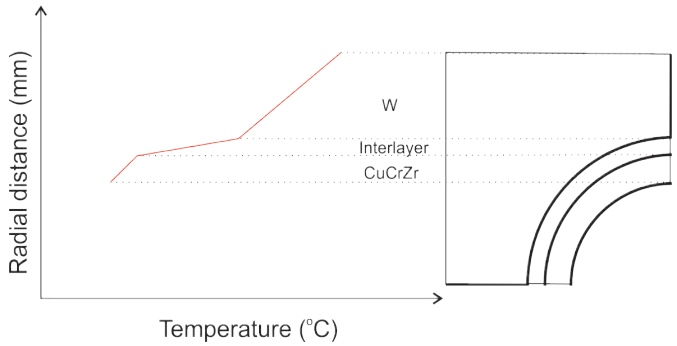

Figure 1.2: Illustration of the thermal barrier concept: temperature vs. radial distance vertically through the divertor target. Note that the temperature gradients are only illustrative.

Barret et al. [6] defined the "optimal" interlayer properties (Young's modulus, CTE and thermal conductivity) using a single design variable termed interlayer copper fraction. This variable is a linear scale factor of the properties for copper. To determine the optimal interlayer properties, other design properties like pipe diameter, tungsten top thickness (above the cooling pipe) and the coolant parameters were kept fixed. The optimal parameters refer to the monoblock design if the design of the system armor material/heat sink changes, the parameters may change was well.

A proposed strategy is the use of WC-Cu interlayer as thermal barrier, since Cu is a good conductor and the composition can be optimized for controls the thermal conductivity. Additionally tungsten carbide (WC) combines favorable properties, such as high hardness, plasticity and good wettability by molten metals [9].

1.3 State of the art

1.3.1 Composite Materials

Metal Matrix Composite Materials are expected to introduce a transition from brittle to ductile behavior if tailoring the properties of the material such as thermal conductivity and CTE from a ceramic-like to a metallic-like behavior by simply adjusting the proportions of the dispersed phase present in the material.

Tungsten monofilament reinforced copper composites (W_f-Cu)

One of the composite materials suggested by Schöbel et al. [10], as a promising interlayer is a W-monofilament reinforced Cu composite (W_f-Cu). These materials combine high temperature strength of W-wires, high thermal conductivity and low CTE. The mismatch stresses (due to the difference in CTE) are transferred to the constituents of the composite material. However, the bonding strength affects strongly the performance of monofilament reinforced composites: if it is too low, interfacial shear stresses between fibers and matrix can cause delamination; severe deformation in the matrix and thermal fatigue during thermal cycling [11] can arise due to the high shear stresses caused by strong bonding between the monofilaments and the matrix. W-wires (140 μm in diameter) were filled parallel into a cylindrical container and consolidated with Cu using hot isostatic pressing (HIP) with 100 MPa at 650 °C. It was found that the mismatch stress in the W-wires between the matrix and the

filaments lead to thermal fatigue damage during thermal cycling. During heating the matrix stress changes from tension to compression due to matrix expansion and during cooling it inverts into a tension state again. At low temperatures the ductility of the matrix is reduced and tensile stresses are responsible for crack formation.

Tungsten wires copper composites produce by vacuum diffusion bonding of monolayers with thickness 130 μm (W wires with 100 μm diameter, Cu foil thickness 60 μm) with volume fractions of W wires between 40% and 55% were developed at the Institute of Materials and Machine mechanics (Slovak academy of sciences) [12]. The materials presented a high thermal conductivity ranging from 200 to 300 $Wm^{-1}K^{-1}$.

FeltMetal™

FeltMetal™ (Technetics Group, USA) is a material consisting of an amorphous of 50 μm diameters copper wires sintered onto a thin copper foil, resulting in a approximately 1 mm thick sheet. Hancock et al. [13] tested two variants of FeltMetal™ with 0.8 and 1 mm thickness. Both variants included silver plating on the Cu fibers. Additional samples with and without silver platting were produced to study the impact of joining methodology. The results were reported as a fraction of the bulk conductivity of copper. For the optimized designs proposed by Barret et al., the ideal values of thermal conductivity of the interlayer must lie between 0.08 and 0.1 of the bulk thermal conductivity of copper. Samples with no additional silver platting presented conductivities close to the ideal ones, while samples with additional platting seems to deteriorate thermal conductivity of the interlayer. Given the promising results of thermal conductivity of FeltMelt™, it would be reasonable to test samples of the same material without silver platting and with different thickness.

Diamond-Copper composites (C_D-Cu)

Another material as interlayer proposed by Shen et al. [14] is a diamond-copper (C_D-Cu) composite. The diamond-reinforced copper was sintered in a vacuum hot pressing furnace with diamond particles of 104-125 μm in diameter. Mock-ups consisting of W/C_D-Cu/CuCrZr were produced using ultra-precision resistance welding. CuCrZr foils at both surfaces of C_D-Cu interlayer were used to cover the weld joints between W and C_D-Cu interlayer. Using infinite element analysis they found that the C_D-Cu interlayer relaxes the stresses from welding interface and avoids crack of the welding interface between components. The mock-up was able to withstood heat fluxes up to 15 $MW.m^{-2}$ without cracking. However, the thermal properties of C_D-Cu composite are expected to change in a fusion reactor due to the formation of a carbon phase with a structure between graphite and diamond which was found after neutron irradiation of natural diamond [15].

1.3.2 Functionally Graded Materials

Functionally graded materials (FGM) are composites characterized by a gradual variation in composition and structure over the material's volume resulting in a gradual change in the material properties according to that variation. This gradual change in properties allows materials to be design

for specific function and applications. Grading a bond interface by gradual material transition is an approach for mitigating thermal stresses in a joint structure. Recently, the concept of W-Cu and W-CuCrZr FGM has been introduced as candidate interlayer material. The content of W in FGM decreases from the W/FGM interface to the FGM/CuCrZr interface as shown in Figure 1.3.

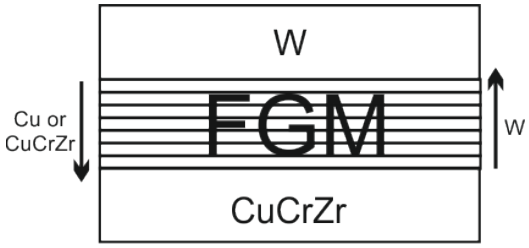

Figure 1.3: Scheme of the functionally graded materials concept. The black arrows indicate the gradient of the element content in the material.

W-Cu and W-CuCrZr FGM have been produced by, infiltration [16], hot pressing [17], resistance sintering [18], hot isostatic pressing [19], spark plasma sintering [20], laser sintering and plasma spraying [21].

W-Cu

Despite the several techniques available to produce FGM, their final properties may vary according to the chosen consolidation technique. For instance, the temperature dependence of CTE and thermal conductivity for W-Cu layers of FGM consolidated by infiltration and plasma sprayed techniques show some differences. Since plasma-sprayed sample presents a layered microstructure the CTE decreases with increasing temperature due to bending of the sample, which is a characteristic bimetal behavior. For the infiltrated composite the reduction in CTE at high temperatures is associated to the relaxation of the Cu phase. According to Pintsuk et al. [21] the CTE and thermal conductivity exhibit lower values for the plasma sprayed sample than for the infiltrated one because of the lack of interconnections between material layers. Despite the two techniques offer good possibilities to form FGM, it was found that an assembly of graded structure is only possible when the starting point is at the Cu side. Vaporization of the Cu particles or delamination due to weak bonding may occur if starting on the W side.

Zhou et al. [22] studied the thermal shock and performance under high heat load of W-Cu FGM produced by plasma spraying, infiltration-welding method and resistance sintering under ultra-high pressure. It was found that the W-Cu FGM materials produced by plasma spraying presented low bonding strength between the coating and the substrate leading to delamination under high heat load (10 MWm^{-2}) tests. No cracks were found in the samples produced by the other two techniques. The FGM produced by ultra-high pressure showed the limitation of being capable of produce only small samples which may restrict its use from an engineering point of view.

However one of the critical drawbacks of a W/Cu FGM is the rapid loss of plastic strength at elevated

temperatures associated to the thermal softening of pure Cu [23].

W-CuCrZr

The thermal and mechanical properties as well the high heat flux tests of W-CuCrZr FGM produced infiltration technique have been studied by You et al. [23] and Greuner et al [16], respectively. The materials produced showed a thermal conductivity with a temperature-independent behavior from room temperature to 600 ºC, indicating a stable behavior of the material in terms of heat transfer. Materials produced under the same conditions were then submitted to heat flux tests. Three mock-ups with W/W-CuCrZr FGM/CuCrZr were tested for heat fluxes ranging from 1 to 15 $MW.m^{-2}$. Despite the mock-ups were successfully cycled up to 15 $MW.m^{-2}$ without any indication of damage, the surface temperature of the W tiles during the tests reached values above the recrystallization temperature of W. The effect of the W/CuCrZr FGM interlayer on temperature, stress and strain distribution in a W/W-CuCrZr FGM/CuCrZr component was examined by Zhu et al. [24] using ANSYS code based on finite element method. The results for this interlayer shown that a thicker one leads to the long heat transfer distance and thus more thermal heat accumulates at surface, causing high surface temperature. Results also revealed that the temperature distribution in the CuCrZr heat sink shows no significant difference independent of the interlayer material used. It is clear that the material selected as interlayer must be able to break the thermal gradient at the joint interfaces while maintaining the heat flow necessary to avoid overheating of the W tiles and heat sink tube.

1.3.3 Cermets

Metal matrix composites have showed promising results as interlayer materials because they can combine properties of the metal matrix and those of the reinforcement phase. This type of materials are expected to introduce the transition from a brittle to ductile behavior if tailoring the properties of the material such as thermal conductivity and CTE from a ceramic-like to a metallic-like behavior by simply adjusting the proportions of the dispersed phase present in the material.

WC-Cu and WC-Co Cermets

WC-metal systems are commonly designated as cemented carbides (or hard metals) and they constitute the most versatile hard materials group for engineering and tooling applications. However, the properties required for the use of these materials as working elements of tools and machine parts differs from those required for an interlayer material. In this sense the term cermet is hereafter used to designate the WC-metal materials. The term cermet is used to designate the WC-metal material and refer to any composite material consisting of ceramic particles bonded with a metallic matrix [25].

Cermets Constituents

Tungsten Carbide

Tungsten and carbon can form two different carbides: WC and W_2C. WC does not melt under standard atmospheric conditions, but decomposes into a liquid phase and graphite above 2780 ºC as shown in the W-C equilibrium phase diagram (Figure 1.4).

The major phase present in cermets (hardmetals) is the monocarbide WC with a hexagonal crystal structure with two atoms per unit cell and a c/a ration of 0.976 [26]. The WC crystals are triangle-shaped therefore many of the properties of individual WC grains are anisotropic. Nevertheless, in the sintered materials no anisotropy is observed due to the random orientation of the grains.

WC grains can undergo some plastic deformation: slip band formation has been observed close to hardness indentations in WC single crystals [27].

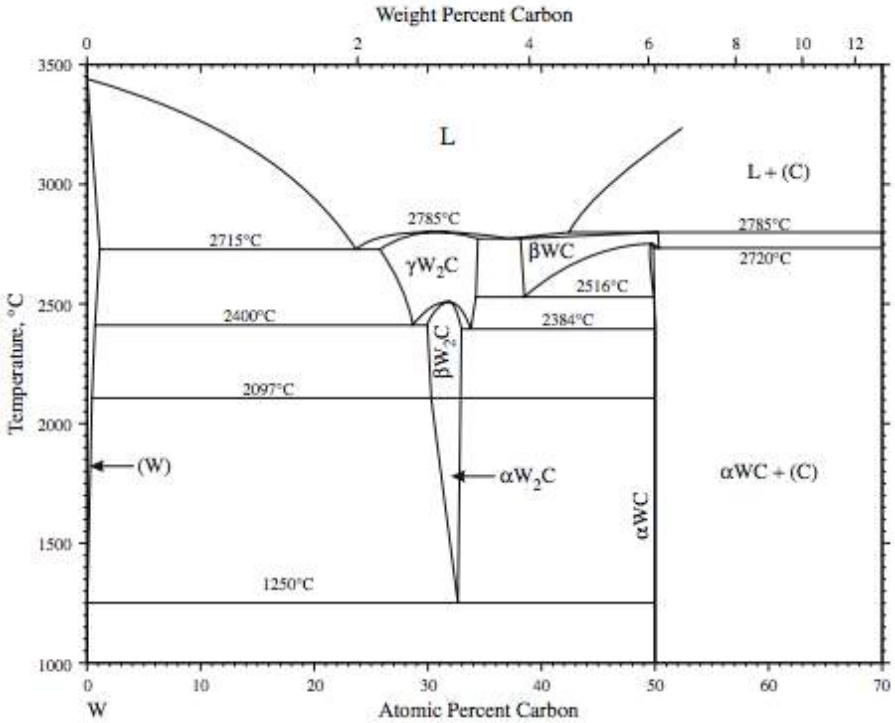

Figure 1.4: W-C phase diagram [28].

Copper-Tungsten phase diagram

The Cu-W equilibrium phase diagram is shown in Figure 1.5. As it can be seen mutual insolubility or negligible solubility between the two species exist. Powder compacts containing only tungsten and copper show very poor sinterability, even by liquid phase sintering above the melting point of the Cu phase [29]. It is known [30] that the fine size and well-mixed state of the component powder improve the sinterability of powder compact, especially in the liquid phase sintering system such as W–Cu system, in which the dominant sintering mechanism is known to be particle rearrangement.

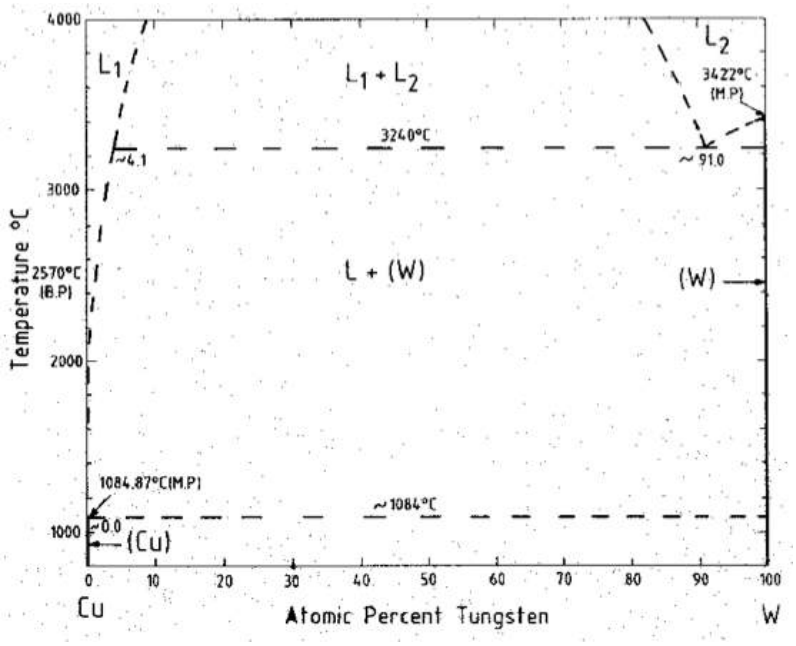

Figure 1.5: Cu-W phase diagram [31].

Copper-Carbon phase diagram

The solubility of C in solid Cu is very small (0.0078 wt.% C) as shown in the Cu-C phase diagram (Figure 1.6). However, the solubility of C is of great practical importance. For example, if even only small amounts of C are dissolved during the production of high-purity noble metals exhibiting very small carbon solubilities, as a consequence of using graphite molds, carbon-oxide gases could be formed when such metals are cast under oxidizing conditions. This could cause gas porosity in e.g. copper-base casting products [32].

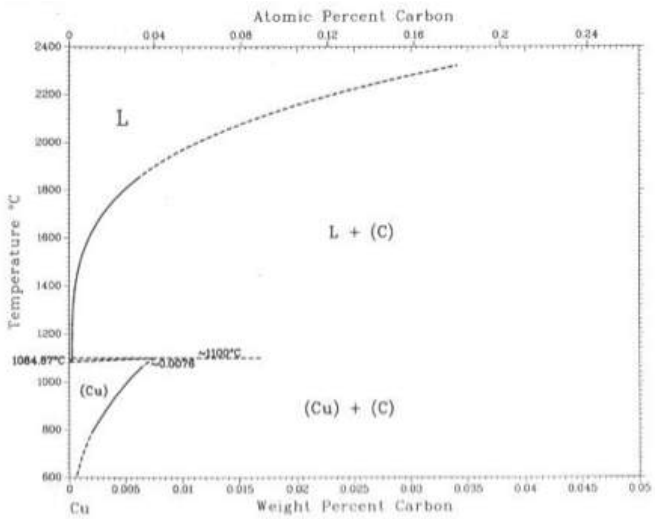

Figure 1.6: Cu-C phase diagram [33].

Cermets production

Copper-based cermets are known for their excellent electrical properties, thermal conductivity and good resistance to oxidation. However, ductility and low wear resistance make some limitation for copper applications. WC-Cu cermets have the advantage of combining the properties of WC and Cu in one single material by adjusting the volume fraction of the dispersed phase (WC) in the Cu matrix. The cermet will possess WC-like properties, such as high hardness and high strength, if the volume content of WC is higher.

WC-Cu cermets have been produced by sintering [34], spark plasma sintering [35], compocasting [36], stir casting [37], infiltration [38], friction stir processing [39], electrodeposition [40] and co-precipitation and carburization processes [41]. The raw/starting materials used to produce WC-Cu cermets may vary from single elemental Cu, W and C (graphite) powders to Cu and WC powders. Yusoff and Hussain [42] studied the effect of sintering parameters on the microstructure of mechanically alloyed copper-tungsten carbide cermets starting with Cu, W and graphite powders as raw materials. The powder mixtures were milled for 40 h at 400 rpm speed with a ball-powder ratio of 10:1 with 10 mm ball. Then, the powders were compacted at 300 MPa and sintered under argon atmosphere at sintering temperatures ranging from 800 to 1000 ºC and holding times of 1 to 3 h. Undesirable phases such as Fe_3W_3C, Cu_2O and $FeWO_4$ were found in the X-rays diffraction patterns of the consolidated materials. The iron contamination resulted from the ball milling during long periods and the formation of oxides is due to the entrapped gas that reacted with the metal powders. It was also found that the amount of WC is dependent on the amount of graphite available and increased with sintering temperature. However, at high temperatures and in the presence of Fe, the amount of WC is reduced due to the formation Fe_3W_3C. The density of the cermets increased with increasing sintering temperature, associated with a reduction of pores.

In fact, the evolution of the structure and phases of the materials during sintering is a concern since the materials properties are dependent on the final microstructure. The hardness and yield strength of copper increases according to Hall-Petch dependence with the grain size decrease [43]. However, at grain size bellow 10 nm, the yield strength commences to decrease with further grain refinement, which is known as inverse Hall-Petch relationship [44]. One of the biggest problems associated with small particles is agglomeration. Particles are very small and are strongly influenced by low order forces (Van der Waals forces) [45]. Strobrawa and Rdzawski studied cermets consisting of WC nanoparticles up to 3 wt. % (1,7 vol. %) dispersed in a nanocrystalline copper matrix [34], [46], [47]. Sintering of the WC and Cu powders was conducted at 570 ºC during 1.5 h in a hydrogen atmosphere. The sintering conditions of copper (without tungsten carbide) did not promote a homogeneous nanostructure in the polycrystalline material. Grain growth to size of several hundred nanometers was observed (the starting grain size ranged from 5 to 45 nm). In the case of the WC-Cu cermets, the grains after sintering (under the same conditions) were below 100 nm in size and highly homogeneous. Nevertheless, the densities achieved were high as 85,8 % and the authors suggest that improvements in density can be possible to accomplish through plastic working.

Another microstructural feature that may influence the behavior of the material is the distribution of the dispersed phase in the matrix. Zhao et al. [48] studied the influence of the powder metallurgy pressing procedure on WC-Cu cermets containing 9 vol. % of WC. The composite powder with an average particle size of 75 μm were compacted under a pressure of 700 MPa and then sintered in a vacuum furnace at 1 x 10^{-4} Torr at 950 ºC for 3 h (stage 1). In a second stage the samples were repressed under 1300 MPa and resintered at 950 ºC for 3 h. In stage 3 the samples were submitted to a second repressing, the samples were rolled 64% in length at room temperature (stage 4). It was found that after repressing and rolling the WC particles dispersion improved. The external force caused the WC particles to re-disperse within the matrix and get more uniform during deformation. The material showed a behavior that varies from brittle-like in stage 1 to a ductile-like in stage 4. In accordance with the studies of Strobrawa and Rdzawski improvements in density and tensile strength of the cermets could be achieve by subsequent processing after sintering.

Achieve high density in order to obtain the best properties that WC-Cu cermets can be quite challenging when producing this type of materials. Near theoretical densities reported in literature refer to WC-Cu cermets produced via processes where molten copper is formed (in contrast to solid state sintering without further plastic working).

Sintered densities close to the theoretical densities can be achieved with micron size particles and high consolidation temperatures and pressure [49]. Deshpande [50] studied the infiltration process of liquid copper in a porous WC preform. He found that infiltration at higher temperatures was facilitated, because the WC has lower conductivity and higher heat capacity than copper. Therefore longer times are required to WC reach the process temperature and the overheating of liquid copper should be high to avoid solidification at the WC/Cu interface, allowing the molten copper to flow.

One of the most studied WC-based cermet is the well-known WC-Co system. These materials are used as working elements of tools and machine parts due to their high wear resistance. The content of Co can vary from 3 to 25 wt. % according to the desired properties. For machining purposes, for instance, alloys with 3 to 12 % Co and WC grain sizes from 0.5 to more than 5 μm are commonly used.

Shinoda et al. [35] compared the consolidation of WC-Cu and WC-Co cermets and the mechanical properties of both materials. The materials containing 16 vol. % Cu and Co binders and without binder were produced via spark plasma. Cobalt addition significantly enhanced the sintering of WC and the consolidation temperature was approximately 1200 ºC, while with the addition of copper temperatures in the order of 1500 ºC are required to achieve the same relative density. The consolidation of WC-Cu is difficult, densified materials can be obtained with the application on an external pressure. The differences in the sintering behavior between WC-Co and WC-Cu cermets can be explained by the kinetics of liquid-phase sintering. In contrast with the WC-Cu system, in the WC-Co system the WC particles are soluble (2 % at 100 ºC [51]) in the liquid cobalt. Solubility of the solid phase (WC) in the liquid phase (metal) is one of the important rate controlling in liquid-phase sintering which influences the stages of liquid-phase sintering. In the initial stage of sintering, wettability of the liquid on the solid particles is improved by a high solubility of the solid phase. This leads to lubrication and smoothening of the particles, which in turn accelerates the rearrangement of particles into a denser configuration

leading to a rapid initial shrinkage [52]. In the intermediate and final stages, the process of solution-precipitation takes place and the solubility of solid phase in the liquid phase is the important rate-controlling factor that determines the densification rate. The difference in solubility of WC in Cu and Co may explain the different mechanical behavior of WC-Cu and WC-Co cermets at high temperatures. Shinoda et al. found that tungsten and carbons atoms dissolve much easily in cobalt than in copper and diffuse very rapidly, i.e., mass transport through the cobalt phase generates creep at elevated temperatures.

Thermal conductivity

The properties of the WC-Co cermets are influenced by the Co content and grain size of the WC. Wang et al. [53] studied the effect of these two variables in the thermal conductivity and CTE of the WC-Co cermets. Thermal conductivity seems to be more sensitive to the WC grain than cobalt content. The authors stated that the scatter in the thermal conductivity and cobalt content relationship may be related to the different W, C solid solutions in the cobalt phase. However, a general trend is evident, i.e., thermal conductivity increases with increasing grain size and decreases with increasing cobalt content. The results achieved by Wang et al. are in accordance with previous works performed in [37, 38].

Despite the properties of WC-Co materials are well known, the variation of thermal conductivity with WC grain size and Cu content in WC-Cu cermets has not been reported so far in literature. Nevertheless, the same tends on the dependence of mechanical and thermal properties of WC-Cu with copper content and WC grain size are expected. For instance, WC presents a higher hardness than copper a decrease in the content of the harder phase results in a decrease of the hardness of the cermet. The opposite trend is found in fracture toughness of the WC-Cu cermets. An increase in fracture toughness with increasing Cu content is observed [35]. Since metals are much more ductile than ceramic, the increase in fracture toughness with increasing metal content is expected because the resistance to crack propagation increase with the ductility of the material [56].

W-Cu thermal conductivity

Thermal conductivity of W-Cu composites was studied by Lee et al. [57]. It was found that the overall thermal conductivity of the composites increased when the copper content increased due to the higher thermal conductivity of the copper phase. The variation of thermal conductivity with temperature is more evident at compositions with more copper and the tendency of thermal conductivity to decrease with increasing temperature can be realized. The inverse proportionality of thermal conductivity with temperature of W-Cu composites was also reported by Kim et al. [58]. The thermal conductivity of the W-Cu composites increased with increasing temperature up to 500 ºC, however with further increase in temperature the thermal conductivity decreased. This dual dependence of thermal conductivity with temperature is due to the contribution of electrons and phonons on thermal conduction. The movements of electrons are affected by structural defects (dislocations, grain boundaries, impurity

atoms, etc.) existing in the materials. For higher temperatures the jumping probability of electrons through the imperfections becomes saturated and the effect of phonons becomes more prominent.

1.4 References

[1] "iter." [Online]. Available: www.iter.org. [Accessed: 24-Sep-2015].

[2] "The ITER Divertor." [Online]. Available: www.iter.org/mach/divertor. [Accessed: 24-Sep-2015].

[3] G. Pintsuk, *Tungsten as a plasma-facing material*, vol. 4. Elsevier Inc., 2012.

[4] G. M. Wright, E. Alves, L. C. Alves, N. P. Barradas, P. a. Carvalho, R. Mateus, and J. Rapp, "Hydrogenic retention of high- *Z* refractory metals exposed to ITER divertor-relevant plasma conditions," *Nucl. Fusion*, vol. 50, no. 5, p. 055004, 2010.

[5] V. Barabash, a. Peacock, S. Fabritsiev, G. Kalinin, S. Zinkle, a. Rowcliffe, J.-W. Rensman, a. a. Tavassoli, P. Marmy, P. J. Karditsas, F. Gillemot, and M. Akiba, "Materials challenges for ITER – Current status and future activities," *J. Nucl. Mater.*, vol. 367–370, no. 2007, pp. 21–32, 2007.

[6] T. R. Barrett, S. C. McIntosh, M. Fursdon, D. Hancock, W. Timmis, M. Coleman, M. Rieth, and J. Reiser, "Enhancing the DEMO divertor target by interlayer engineering," *Fusion Eng. Des.*, 2015.

[7] I. Smid, M. Akiba, G. Vieider, and L. Plöchl, "Development of tungsten armor and bonding to copper for plasma-interactive components," *J. Nucl. Mater.*, vol. 258–263, no. 1998, pp. 160–172, 1998.

[8] J. . Davis and G. . Kalinin, "Material properties and design requirements for copper alloys used in ITER," *J. Nucl. Mater.*, vol. 258–263, pp. 323–328, 1998.

[9] R. Gassmann, "Laser cladding with (WC + W2C)/Co-Cr-C and (WC + W2C)/Ni-B-Si composites for enhanced abrasive wear resistance," *Mater. Sci. Technol.*, vol. 12, no. August, pp. 691–696, 1996.

[10] M. Schöbel, J. Jonke, H. P. Degischer, V. Paffenholz, a. Brendel, R. C. Wimpory, and M. Di Michiel, "Thermal fatigue damage in monofilament reinforced copper for heat sink applications in divertor elements," *J. Nucl. Mater.*, vol. 409, no. 3, pp. 225–234, 2011.

[11] S. Kimmig, S. Elgeti, and J. H. You, "Impact of long-term thermal exposure on a SiC fiber-reinforced copper matrix composite," *J. Nucl. Mater.*, vol. 443, no. 1–3, pp. 386–392, 2013.

[12] "Metal matrix composites." [Online]. Available: http://www.umms.sav.sk/index.php?ID=1088. [Accessed: 02-Oct-2015].

[13] D. Hancock, T. Barrett, J. Foster, M. Fursdon, G. Keech, S. McIntosh, W. Timmis, M. Rieth, and J. Reiser, "Testing candidate interlayers for an enhanced water-cooled divertor target," *Fusion Eng. Des.*, 2015.

[14] W. Shen, P. Li, C. Zhou, S. Xu, and S. Wang, "WATER-COOLED PLASMA-FACING MOCKUPS WITH DIAMOND / COPPER COMPOSITE INTERLAYER," *Fusion Sci. Technol.*, vol. 66, 2014.

[15] V. . Blank, V. . Aksenenkov, M. Y. Popov, S. . Perfilov, B. . Kulnitskiy, Y. . Tatyanin, O. . Zhigalina, B. . Mavrin, V. . Denisov, a. . Ivlev, V. . Chernov, and V. . Stepanov, "A new carbon structure formed at MeV neutron irradiation of diamond: structural and spectroscopic investigations," *Diam. Relat. Mater.*, vol. 8, no. 7, pp. 1285–1290, 1999.

[16] H. Greuner, A. Zivelonghi, B. Böswirth, and J.-H. You, "Results of high heat flux testing of W/CuCrZr multilayer composites with percolating microstructure for plasma-facing components," *Fusion Eng. Des.*, pp. 2–5, 2015.

[17] P. Zhao, S. Wang, S. Guo, Y. Chen, Y. Ling, and J. Li, "Effects of temperature and holding time on bonding W and W-Cu composites with an amorphous W-Fe coated copper foil as the interlayer by hot-pressing," *J. Nucl. Mater.*, vol. 438, no. 1–3, pp. 72–76, 2013.

[18] M. Takahashi, Y. Itoh, M. Miyazaki, H. Takano, and T. Okuhata, "Fabrication of Tungsten / Copper Graded Material," vol. 12, pp. 243–250, 1994.

[19] A. Herrmann, H. Greuner, M. Balden, and H. Bolt, "Design and evaluation of an optimized W/Cu interlayer for W monoblock components," *Fusion Eng. Des.*, vol. 86, no. 1, pp. 27–32, 2011.

[20] E. Autissier, M. Richou, L. Minier, J.-L. Gardarein, and F. Bernard, "Elaboration and thermomechanical characterization of W/Cu functionally graded materials produced by Spark Plasma Sintering for plasma facing components," *Fusion Eng. Des.*, 2015.

[21] G. Pintsuk, S. E. Brünings, J. E. Döring, J. Linke, I. Smid, and L. Xue, "Development of W/Cu-functionally graded materials," *Fusion Eng. Des.*, vol. 66–68, pp. 237–240, 2003.

[22] Z. J. Zhou, S. X. Song, J. Du, Z. H. Zhong, and C. C. Ge, "Performance of W/Cu FGM based plasma facing components under high heat load test," *J. Nucl. Mater.*, vol. 363–365, no. 1–3, pp. 1309–1314, 2007.

[23] J. H. You, a. Brendel, S. Nawka, T. Schubert, and B. Kieback, "Thermal and mechanical properties of infiltrated W/CuCrZr composite materials for functionally graded heat sink application," *J. Nucl. Mater.*, vol. 438, no. 1–3, pp. 1–6, 2013.

[24] D. H. Zhu, J. L. Chen, Z. J. Zhou, and R. Yan, "Thermal-mechanical analysis on W/CuCrZr plasma facing component with functionally graded material interlayer," *J. Phys. Conf. Ser.*, vol. 419, p. 012038, 2013.

[25] E. B. Sebok and R. L. Taylo, *Concise Encyclopedia of Composite Materials*, Second. Elsevier, 2007.

[26] H. E. Exner, "Physical and chemical nature of cemented carbides," *Int. Met. Rev.*, vol. 24, no. 1, pp. 149–173, 1979.

[27] D. N. French and D. A. Thomas, "Hardness anisotropy and slip in WC crystals," *Trans. Met. Soc. AIME*, vol. 233, pp. 950–952, 1965.

[28] H. Okamoto, "C-W (Carbon-Tungsten)," *J. Phase Equilibria Diffus.*, vol. 29, no. 6, pp. 1–2, 2008.

[29] W. D. Kingery, "Densification during Sintering in the Presence of a Liquid Phase. I. Theory," *J. Appl. Phys.*, vol. 30, 1959.

[30] S. S. Ryu, Y. D. Kim, and I. H. Moon, "Dilatometric analysis on the sintering behavior of nanocrystalline W-Cu prepared by mechanical alloying," *J. Alloys Compd.*, vol. 335, no. 1–2, pp. 233–240, 2002.

[31] P. R. Subramanian and D. E. Laughlin, "Copper-Tungsten," *Phase Diagrams of Binary Tungsten Alloys*. pp. 76–79, 1991.

[32] G. A. López and E. J. Mittemeijer, "The solubility of C in solid Cu," *Scr. Mater.*, vol. 51, no. 1, pp. 1–5, 2004.

[33] K. M. Zwilsky and E. L. Langer, *ASM Handbook Volume 3: Alloy Phase Diagrams*, vol. 3, no. 3. ASM International, 1982.

[34] J. P. Stobrawa and Z. M. Rdzawski, "Dispersion-strengthened nanocrystalline copper," *J. Achiev. Mater. Manuf. Eng.*, no. 2, pp. 35–42, 2007.

[35] Y. Shinoda, Y. Yanagisawa, T. Akatsu, F. Wakai, and H. Fujii, "Development of Creep-Resistant Tungsten Carbide Copper Cemented Carbide," *Mater. Trans.*, vol. 50, no. 6, pp. 1250–1254, 2009.

[36] K. Ichikawa and M. Achikita, "Electric conductivity and mechanical properties of carbide dispersion strengthened copper prepared by compocasting," *Mater. Trans.*, vol. 34, pp. 718–724, 1993.

[37] B. M. Girish, B. B., B. M. Satish, and D. R. Somashekar, "Electrical Resistivity and Mechanical Properties of Tungsten Carbide Reinforced Copper Alloy Composites," *Int. J. Compos. Mater.*, vol. 2,

no. 3, pp. 37–43, 2012.

[38] E. Hong, B. Kaplin, T. You, M. S. Suh, Y. S. Kim, and H. Choe, "Tribological properties of copper alloy-based composites reinforced with tungsten carbide particles," *Wear*, vol. 270, no. 9–10, pp. 591–597, 2011.

[39] J. Khosravi, M. K. B. Givi, M. Barmouz, and A. Rahi, "Microstructural, mechanical, and thermophysical characterization of Cu/WC composite layers fabricated via friction stir processing," *Int. J. Adv. Manuf. Technol.*, vol. 74, no. 5–8, pp. 1087–1096, 2014.

[40] V. Medeliene and A. Kosenko, "Structural and Functional Properties of Electrodeposited Copper Metal Matrix Composite Coating with Inclusions of WC," *Mater. Sci.*, vol. 14, no. 1, pp. 29–33, 2008.

[41] M. a Rdestani, H. a Rabi, H. R. Azavizadeh, H. R. R. Ezaie, and H. M. Ehrjoo, "Synthesis of WC – 20 wt . % Cu composite powders by co-precipitation and carburization processes," vol. 28, no. 2, 2010.

[42] M. Yusoff and Z. Hussain, "Effect of Sintering Parameters on Microstructure and Properties of Mechanically Alloyed Copper-Tungsten Carbide Composite," *Int. J. Mater. Mech. Manuf.*, vol. 1, no. 3, pp. 283–286, 2013.

[43] S. Cheng, E. Ma, Y. M. Wang, L. J. Kecskes, K. M. Youssef, C. C. Koch, U. P. Trociewitz, and K. Han, "Tensile properties of in situ consolidated nanocrystalline Cu," *Acta Mater.*, vol. 53, no. 5, pp. 1521–1533, 2005.

[44] H. Conrad, "Grain size dependence of the plastic deformation kinetics in Cu.pdf," vol. 341, pp. 216–228, 2003.

[45] S. H. Yoo, T. S. Sudarshan, K. Sethuram, G. Subhash, and R. J. Downding, "Consolidation and High Strain Rate Mechanical Behavior of Nanocrystalline Tantalum," *NanoStructured Mater.*, vol. 12, no. 99, pp. 23–28, 1999.

[46] J. P. Stobrawa and Z. M. Rdzawski, "Characterisation of nanostructured copper - WC materials," *J. Achiev. Mater. Manuf. Eng.*, vol. 32, no. 2, pp. 171–178, 2009.

[47] J. P. Stobrawa and Z. M. Rdzawski, "Deformation behaviour of dispersion hardned nanocrystalline copper," *J. Achiev. Mater. Manuf. Eng.*, vol. 17, no. 1–2, pp. 153–156, 2006.

[48] N. Zhao, J. Li, and X. Yang, "Influence of the P/M process on the microstructure and properties of WC reinforced copper matrix composite," *J. Mater. Sci.*, vol. 39, no. 15, pp. 4829–4834, 2004.

[49] A. UPADHYAYA and R. M. GERMAN, "Densification and dilation of sintered W-CU alloys," *Int. J. powder Metall.*, vol. 34, no. 2, pp. 43–55.

[50] P. K. Deshpande, "Wear Resistance and Electrical Property of Infrared Processed Copper/Tungsten Carbide Composites," University of Cincinnati, 2006.

[51] W. A. Glaeser, *Materials For Tribology*. Elsevier, 1992.

[52] R. M. German, *Liquid Phase Sintering*, First. Plenum Press New York, 1985.

[53] H. Wang, T. Webb, and J. W. Bitler, "Study of thermal expansion and thermal conductivity of cemented tungsten carbide," *Present. ICSHM10 Submitt. Publ.*, 2014.

[54] W. Q. Cao, G. F. Dirras, M. Benyoucef, and B. Bacroix, "Room temperature deformation mechanisms in ultrafine-grained materials processed by hot isostatic pressing," *Mater. Sci. Eng. A*, vol. 462, no. 1–2, pp. 100–105, 2007.

[55] W. Neumann, "Thermal diffusivity of cemented carbides," in *Thermal Conductivity 18*, 1st ed., T. Ashworth and D. R. Smith, Eds. Springer US, 1984, pp. 473–481.

[56] J. L. Chermant and F. Osterstock, “Fracture toughness and fracture of WC-Co composites,” *J. Mater. Sci.*, vol. 11, no. 10, pp. 1939–1951, 1976.

[57] S. H. Lee, S. Y. Kwon, and H. J. Ham, “Thermal conductivity of tungsten-copper composites,” *Thermochim. Acta*, vol. 542, pp. 2–5, 2012.

[58] Y. Do Kim, N. L. Oh, S. T. Oh, and I. H. Moon, “Thermal conductivity of W-Cu composites at various temperatures,” *Mater. Lett.*, vol. 51, no. 5, pp. 420–424, 2001.

2. Experimental Techniques and Procedure

This chapter is divided in two sections related to the experimental techniques used in this work. In the first section the reader will find a brief description of the techniques used in this work as well as the physical and mathematical principles behind those techniques. In the second section a detailed description of the experimental procedure can be found.

2.1 Experimental Techniques

2.1.1 Hot Pressing

Hot pressing (HP) is a technique, which combines powder pressing and sintering into one single operation. By applying temperature and pressure simultaneously it is possible to achieve near theoretical density in a wide range of materials. Figure 2.1 shows a scheme of a hot pressing unit. A typical hot pressing procedure can be summarized in six steps:

(i) Introduction of the powder mixture or cold compacted preform into the mold;
(ii) The mold is heated to a specific temperature by induction or resistance methods;
(iii) Pressuring the powder;
(iv) Rising the temperature during compacting at a certain rate until a specific temperature;
(v) Application of temperature and pressure during a dwell time;
(vi) Cooled down of the mold, under pressure, to room temperature.

HP takes advantage of the loss of resistance to plastic deformation by metal particles with increase in temperature, as a result, much lower pressures are needed to consolidate the material. The pressure applied by a uniaxial press can range from 20 to 50 MPa for a graphite die.

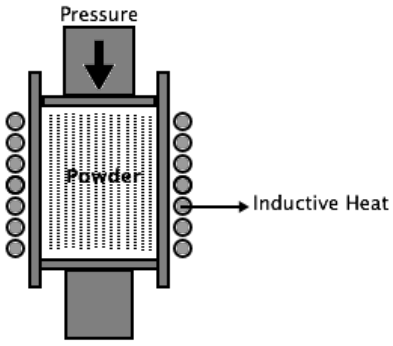

Figure 2.1: Scheme of a hot pressing unit.

The parameters that control the quality of a hot pressed material are the pressure, temperature, time and the working atmosphere. In fact, pressure increases the driving force densification, reducing the processing temperature required for a sintering process. Despite of HP being capable of achieve near theoretical density, it introduces limitations to available specimen geometries. In some applications machining operations are required which can be quite expensive. Another parameter conditioning the

hot pressing procedure is the ratio H/D, where H is the height and D the diameter of a cylindrical section of the specimen [1]. Pressing becomes difficult as the value of the ratio H/D increases; for ratios between 1 and 3 can cause problems with die wall friction, ram motion, and pressure distribution which can affect the microstructure homogeneity (density) of the specimen. [2].

2.1.2 Scanning Electron Microscopy

Scanning electron microscopy (SEM) is a versatile characterization technique capable of providing information about morphology, topography, compositional differences, crystal structure and its orientation. The main characteristics of SEM that makes it such powerful technique are the multiple signals generated (such as secondary electrons, backscattered electrons and X-rays), the simple process that is the image formation, the wide magnification range (bellow 50x to over 100 000x), and good depth of field. The principal components of a SEM are: the electron gun, magnetic lenses, scanning coils, and detectors as shown in Figure 2.2. The electron gun is responsible for the emission and acceleration of electrons. There are two types of electron guns: the thermionic electron and field emission. In thermionic electron guns a current passes through a filament (tungsten or lanthanum hexaboride) causing the filament to heat and thermionic electrons are emitted from the filament. In field emission gun a negative potential is applied at the tip of a tungsten cathode. When the field reaches a magnitude of 10 V/nm the potential barrier of the electrons to be emitted becomes so narrow and lower (in height) that electrons are able to “tunnel” through it and can be emitted by the cathode [3]. In comparison with the thermionic gun, field emission guns need to operate at higher levels of vacuum and are more expensive, but they provide much higher brightness and higher resolution. The magnetic lenses are used to positioning and focusing the electron beam. These lenses consist in coils that generate an electromagnetic field and their function is to reduce the diameter of the electron beam produced by the electron gun in order to achieve high resolution. The scan coils control the position of the beam producing the image, determining magnification, electronic shifting of the area of interest (imaged area), and positioning a probe for X-ray analysis.

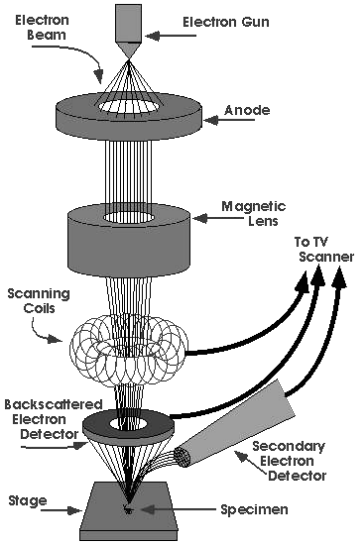

Figure 2.2: Scheme of a Scanning Electron Microscope [4].

The interaction of the electron beam with the specimen produces different signal types emitted by the specimen as secondary electrons (SE), backscattered electrons (BSE), characteristic X-rays, and light (cathodoluminescence). SE, BSE and X-rays signals are those of most interest because these signals are generated from specific volumes within the specimen and can be used to examine different characteristics of the specimen such as composition, crystallography and surface topography.

BSE are primary electrons reflected from the sample by elastic scattering, i.e. they conserve their kinetic energy during collisions but their direction of propagation is modified. BSE present typically energy of the order of 0.5 of the energy of the primary electron beam (E_0) as shown in Figure 2.3. These electrons can emerge from volumes deeper in the sample and their emission is sensitive to the atomic number and therefore the imaging resulting from BSE signal is able to reveal contrast between phases with different compositions. Due to the high energy of BSE their trajectory cannot be changed with an external potential, otherwise some perturbations would be induced in the primary electron beam. In order to maximize the collection of BSE the detector is placed concentrically around the beam and directly above the sample with no bias applied.

When the electrons from the primary electron beam strikes the sample they will loose kinetic energy which will be transferred to the electrons of the sample – inelastic interactions. SE electrons are loosely bounded from the sample atoms that are ejected from the atom because they receive sufficient kinetic energy during inelastic scattering of the beam electrons. Since SE are defined based on the kinetic energy, all electrons emitted from the sample with energy less than 50 eV are considered SE. Due to their low energy it is possible to collect a high fraction of SE by biasing the detector to a modest positive potential (10kV). SE electrons are responsible for the topographic contrast of the image. The contrast difference between SE and BSE images is that the bright regions in a BSE image correspond to the presence of heavier elements, whereas the bright regions in a SE image correspond to hills.

Some of the disadvantages of SEM include: the need of high vacuum environment of the sample, which can be difficult to achieve with porous materials and can even cause the damaging of some biological samples; the samples need to be conductive to avoid charging that can affect the signal

detention and the primary beam. If the samples are not conductive they must be covered with a metal (or carbon) thin layer to provide the electrical conductivity required for good imaging.

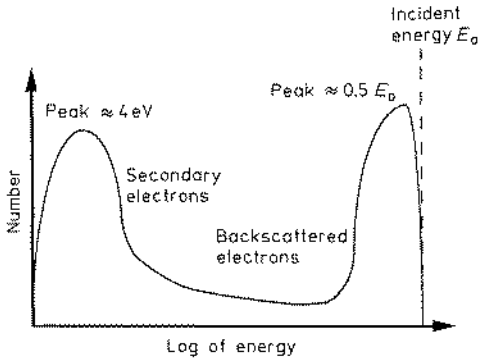

Figure 2.3: Schematic plot of the energy distribution of electrons emitted from a sample in SEM [5].

2.1.3 Energy dispersive X-ray spectroscopy

Energy dispersive X-ray spectroscopy (EDS) is a technique coupled with electron microscopy, capable of detecting X-rays resulting from the interaction of the primary beam with the atoms present in sample. When a high-energy electron (primary beam) ionizes an inner shell electron, a “hole” is created. This hole is than filled by an outer shell electron, this transition between inner atomic energy levels causes the emission of a characteristic X-ray.

The main component of an EDS equipment is a solid-state detector, consisting of a semiconductor. When the X-ray photon hits the detector knocking out electrons from the semi-conductor produces a very small current. The energy of the X-ray photon can be determined by measuring the amount of current produced. A multi-channel analyzer measures the pulse height of the electrical impulse. The pulse’s height is converted into a specific channel address. A histogram of X-ray counts versus X-ray energy containing the peaks corresponding to the elements present in the sample forms an EDS spectrum. The higher the peak present in the spectrum the higher is the element fraction in the sample. Nevertheless, when performing a quantitative analysis some cautions are needed such as background removal and peak deconvolution. Correction of the peak intensities due to matrix effects is needed for a semi-quantitative analysis. There are three matrix effects that can be corrected according to theoretical models:

(i) Atomic Number correction: The probability of production of an X-ray by an incident electron depends on the probability of backscattering and on the average depth of X-ray production, which depend upon the beam voltage and average atomic number of the sample.

(ii) Absorption correction: The probability of an X-ray exiting the sample and reach the detector depends upon the absorption of the surrounding elements. Each element is characterized by a set of absorption coefficients for X-rays of various energies, and the overall absorption for a specific energy depends on the composition of the sample as well as on the path length of the exiting X-ray.

(iii) Fluorescence correction: A second element in the matrix may be excited and decay with emission of its characteristic X-ray by absorbing a emitted characteristic X-ray from a primary matrix element – secondary fluorescence. This process results in an intensity enhancement for the fluorescent element and an associated decrease in intensity of the primarily excited atom.

For a quantitative analysis samples of known composition are used as standards and the concentration of an element can be inferred from the ratio between the peaks of the sample and the peaks of the standard (for each element). X-ray maps can be recorded simultaneously using image brightness intensity as a function of the local relative concentration of each element present.

2.1.4 Vickers Hardness Testing

Hardness is a measure of resistance of a solid material to deformation when a compressive force is applied. The first test for measure hardness was based on natural minerals called Mohs test, which consists in the ability of a mineral to scratch another softer mineral. The Mohs scale offers a qualitative evaluation of hardness that varies from 1 to 10, where 1 represents the minerals that are scratched by talc and 10 the minerals scratched by diamond. Nowadays there are tests that allow a quantitative analysis of hardness based on the resistance of the material to penetration of an indenter. Small or shallow indentations will result if the material is hard, whereas a large or deep indentation will result if the material is soft. Quantitative tests are often classified according to the extent of the test force applied or by measuring method used. A “macro” test refers to a test where a load superior to 1 kg is applied, whereas a “micro” tests refers to a test where a load less than 1 kg of force is applied. Some instruments are capable of conducting tests with loads in the order of 0.01 g referred as nano indentation testers.

Brinell and Rocwell testers are used measuring macro hardness, while Knoop testers are used to measure micro hardness. Vickers testers are used for both micro and macro hardness. The measure of the indentation diameter (Vickers, Brinell and Knoop) or the indentation depth (Rockwell) is required to attribute the value of hardness. It should be pointed that hardness is not a fundamental material property but its testing is considered a useful tool to evaluate the “quality” of a material [6]. A preliminary fracture toughness evaluation can be based on the observations of cracks surrounding the indentation. The Vickers method to measure hardness uses a square pyramid indenter made of diamond. The angle of the indenter is 136^{o}. A normally load is applied during a given time (10 to 15 seconds) in the indenter according to Figure 2.4 causing the material to yield.

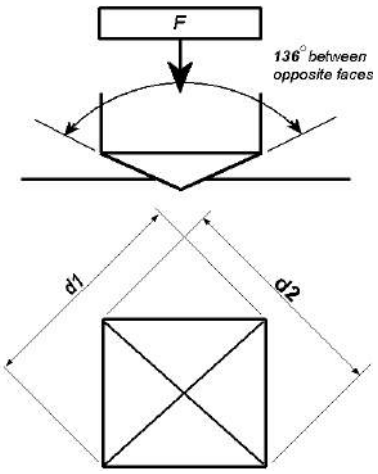

Figure 2.4: Scheme of a Vickers indenter [7].

The two diagonals of the indentation in the surface of the material after removal of the load are measured using a microscope. The hardness value is determined by the amount of permanent

deformation relative to the initial load applied (F). The area (A) of the indentation can quantify the deformation caused by the indenter and is given by:

$$A = \frac{d^2}{2\sin\left(\frac{136}{2}\right)} \tag{2.1}$$

Where d is the mean of the diagonals of the indentation left in the material. The Vickers Hardness (HV) in kgf/mm^2 is

$$HV = \frac{F}{A} = \frac{2\sin\left(\frac{136}{2}\right)F}{d^2} \approx \frac{1.8544F}{d^2} \tag{2.2}$$

It is usual to report HV in the SI units of pressure MPa and GPa. The Vickers hardness is denoted by the symbol HV preceded by the hardness value and followed by the number representing the test force and the duration of loading (in seconds). Vickers Hardness tests are considered independent of the test load which means that when applying different load in a homogeneous material the HV measured is almost the same [8]. Sample materials to be tested must be fine polished in order to avoid interference between the surface deformation and scratches and the ability of the operator to determine the diameter of the indentation. Another important feature is the distance between indentations, because when the material is deformed, the surroundings of the indentation are disturbed and may undergo work hardening. According to ISO 6501-1 [9] the minimum spacing between the centers of two indentations shall be at least three times the mean diagonal length of the indentation in the case of copper and copper alloys.

2.1.5 Thermal diffusivity by the laser flash technique

Diffusivity is a measure of how fast can a material change its temperature: it increases with the ability of the material to conduct heat (λ) and decreases with the amount of heat need to change the temperature of the material by 1K (C_p). The thermal diffusivity of a material determined by the laser flash technique is based on the thermal response of the rear face of an adiabatically insulated material disk whose front side was exposed to a pulse of radiant energy (e.g. laser) (Figure 2.5). The process of measuring the thermal diffusivity involves the heating of one side of a material's disk and acquiring the temperature rise curve on the opposite side of the disk. The time that heat takes to travel through the sample and cause the temperature to rise on the rear face can be used to measure the diffusivity and thermal conductivity if the specific heat and density are known [8] .

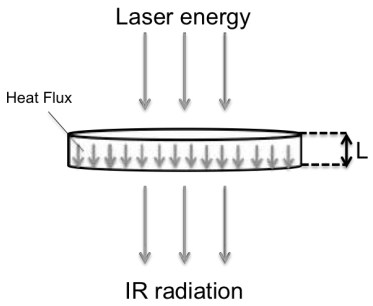

Figure 2.5: Scheme of the laser flash technique.

Thermal diffusivity (α) and conductivity (λ) are related with the equation:

$$\alpha = \frac{\lambda}{C_p \rho} \tag{2.3}$$

where C_p and ρ are specific heat and density, respectively. The thermal diffusivity is measured with a Laser Flash FL 5000 apparatus. This equipment (Figure 2.6) is composed by: (i) a sample holder, (ii) a furnace or a cooler that allows conservation and record of the sample reference temperature; (iii) a vacuum-tight enclosure equipped with two windows for the laser and the detector; (iv) a pulse laser; (v) a system for measuring and recording the rear face temperature transient; (vi) a power supply for the furnace or cooling unit; (vii) an adequate vacuum system; (viii) and a computer to control the experiment, data acquisition, and subsequent data processing. The sample disk has a standard diameter of 12.7mm and its thickness can vary from 1 to 7 mm. In the apparatus the disk is aligned between a laser and a pyrometer in a furnace. A pyrometer controls the temperature of the disk ant its surroundings. When the sample is at the stabilized desired temperature, the laser strikes the sample several times over a specific time interval and the data is recorded for each time the laser strikes the sample. A thin surface layer at the front surface of the disk absorbs the energy of the laser beam causing a heat pulse to travel trough the direction of the samples' thickness. Some devices have two detectors for measurements at different temperatures; for instance, InSb detector may be used for measurements up to 500 ^{o}C and a photo diode for detections from 500 to 2200 ^{o}C. The temperature rise vs. time is amplified and recorded with a high speed A/D converter. Vacuum and/or gas enclosures prevent heat exchange between the sample and the surrounding environment.

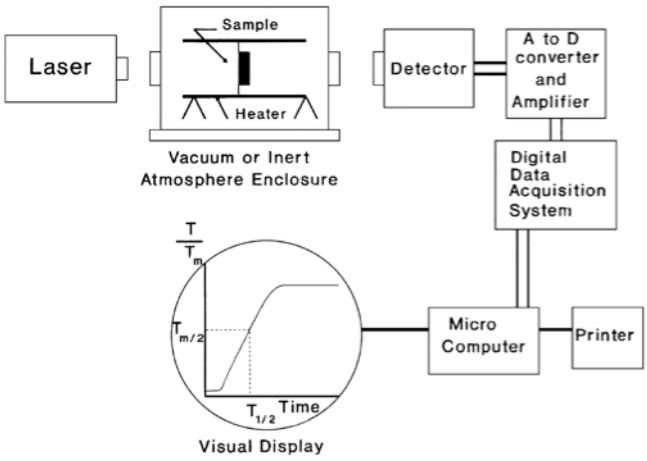

Figure 2.6: Scheme view of a laser flash apparatus a laser flash apparatus and a typical temperature rise curve [8].

In the case of the material being transparent to infrared radiation it is necessary to coat the sample on both sides with a metal film. This prevents the laser beam penetration in the sample on the front side and also events the viewing of the IR detector into the sample on the backside. The front side of the sample should be polished (if possible) to reduce interferences between the laser and surface irregularities that can interfere in the results.

The heat balance equation for transient conditions that describes the system for which the thermal diffusivity is to be determined may be written, using Fourier's first law, as

$$\nabla\lambda\nabla T + g(r,t) = C_p\rho\frac{\partial T}{\partial t} \tag{2.4}$$

where g(r,t) represents the internal sources and sinks of heat, $\nabla\lambda$ and ∇T represent the gradient of thermal conductivity and temperature over the material disk, respectively, and $\frac{\partial T}{\partial t}$ correspond to the rate of change in temperature. If one considers there is no such internal sources and sinks and that thermal conductivity is independent of the temperature then

$$\lambda\nabla^2 T = C_p\rho\frac{\partial T}{\partial t} \tag{2.5}$$

The physical model to determine thermal diffusivity by Laser Flash assumes:

(i) Infinitely short pulse;
(ii) One-dimensional heat flow normal to the plate face;
(iii) Adiabatic conditions on both plate faces;
(iv) Uniform distribution of energy over the pulse;
(v) Pulse absorption in a very thin layer of the specimen;
(vi) Homogeneous material;
(vii) Properties of materials are constant within the range of analysis.

Taking in account equation 1 and considering that the disk is infinite in two dimensions but finite in thickness, the heat equation in the thickness direction can be written as

$$\frac{\partial T}{\partial t} = \alpha\frac{\partial^2 T}{\partial x^2} \tag{2.6}$$

Equation 4 is also referred to as Fourier's second law of heat conduction. This equation is a special case of the heat equation since it assumes one-dimensional conduction in a planar medium with constant properties and no generation of heat. Thus, equation 4 states that the rate of change in temperature $\left(\frac{\partial T}{\partial t}\right)$ is proportional to the net transfer of thermal energy in the thickness' direction $\left(\alpha \frac{\partial^2 T}{\partial x^2}\right)$. The adiabatic conditions at the faces of a disk with thickness L give rise to the following boundary conditions

$$\frac{dT}{dx}(0,t) = \frac{dT}{dx}(L,t) = 0, \qquad t > 0 \tag{2.7}$$

Such conditions state that there is no heat transference between the faces of the disk and their surroundings. The solution of equation 4 that gives the temperature (T) at given time (t) at a position x in the disk can be find using the method of separation of variables

$$T(x,t) = C_0 + \sum_{n=1}^{\infty} C_n \, e^{\left(-\frac{\pi^2 n^2 \alpha t}{L^2}\right)} \cos\left(\frac{n\pi x}{L}\right) \tag{2.8}$$

Where C_0 and C_n are constants that must be determined using the initial conditions of temperature distribution in the disk at t=0. The temperature distribution resulting from a short pulse of energy Q emitted by the laser and absorbed by the disk over a thin surface layer of thickness g is expressed by the function f in the following way

$$f(x) = \begin{cases} \dfrac{Q}{\rho C_p g}, 0 \le x \le g \\ 0, \qquad g < x < L \end{cases} \tag{2.9}$$

Then the temperature at t=0

$$T(x,0) = C_0 + \sum_{n=1}^{\infty} C_n \cos\left(\frac{n\pi x}{L}\right) = f(x) \tag{2.10}$$

And the constants C_0 and C_n are determined by

$$C_0 = \frac{1}{L}\int_0^g \frac{Q}{\rho C_p g}\, dx = \frac{Q}{\rho C_p L} \tag{2.11}$$

$$C_n = \frac{2}{L}\int_0^g \frac{Q}{\rho C_p g} \cos\left(\frac{n\pi x}{L}\right) dx = \frac{2}{L}\frac{Q}{\rho C_p L}\frac{L}{n\pi g} \sin\left(\frac{\pi n g}{L}\right) \tag{2.12}$$

For opaque solids the energy pulse Q is absorbed at a very thin layer, meaning that the ration g/L is sufficiently small and the approximation $\sin\left(\frac{\pi n g}{L}\right) \approx \frac{\pi n g}{L}$ is valid and equation 9 can be simplified. Substituting in equation 6 the expressions for C_0 and C_n obtained in equation 8 and 9 gives

$$T(x,t) = \frac{Q}{\rho C_p L}\left[1 + 2\sum_{n=1}^{\infty} e^{\left(-\frac{\pi^2 n^2 \alpha t}{L^2}\right)} \cos\left(\frac{n\pi x}{L}\right)\right] \tag{2.13}$$

To access the thermal diffusivity it is need to estimate the temperature at the rare face, i.e., the temperature at a given time t at x=L. Taking in account that

$$\sum_{n=1}^{\infty} \cos\left(\frac{n\pi L}{L}\right) = \sum_{n=1}^{\infty} \cos(n\pi) = \sum_{n=1}^{\infty} (-1)^n \tag{2.14}$$

Equation 10 can be simplified and used to estimate the temperature at rare face of the disk

$$T(L,t) = \frac{Q}{\rho C_p L}\left[1 + 2\sum_{n=1}^{\infty}(-1)^n e^{\left(-\frac{\pi^2 n^2 \alpha t}{L^2}\right)}\right] \quad (2.15)$$

Equation 12 gives the temperature at the rear face of the disk at a given time t, however after a infinite time the temperature at the rear face will be reduce to:

$$T(L, t \to \infty) = \frac{Q}{\rho C_p L} = T(L, max) \quad (2.16)$$

This means that the maximum rear face temperature is a function of the energy pulse of the laser (Q), density (ρ), specific heat (C_p) and thickness of the disk material (L). For practical applications it is common to relate thermal diffusivity (α) to the percent rise in the rear face temperature V(L,t):

$$V(L,t) = \frac{T(L,t)}{T(L,max)} = 1 + 2\sum_{n=1}^{\infty}(-1)^n e^{\left(-\frac{\pi^2 n^2 \alpha t}{L^2}\right)} \quad (2.17)$$

By plotting the percent rise in the rear face temperature of the disk (V(L,t)) versus the quantity $\frac{\pi^2 \alpha t}{L^2}$ as shown in Figure 2.7 it is easy to understand how thermal diffusivity of the disk material can be determined. Parker et al. [10] selected the point corresponding to 50% (0.5) of the maximum temperature to access thermal diffusivity. The value of the quantity $\frac{\pi^2 \alpha t}{L^2}$ corresponding to 50% of the maximum temperature is 1.38 (Figure 2.7). In this case

$$V(L,t) = 0.5 \Rightarrow \frac{\pi^2 \alpha t_{0.5}}{L^2} = 1.38 \Leftrightarrow \alpha = \frac{1.38 L^2}{\pi^2 t_{0.5}} \quad (2.18)$$

Where $t_{0.5}$ is the time required to the rear face temperature reach 50% of its maximum temperature. Nevertheless, other points of temperature rise can be chosen in order to determine thermal diffusivity. In that case the thermal diffusivity (α) of the sample related to any percent rise in temperature and the sample thickness (L) is given by

$$\alpha = K_y \frac{L^2}{t_y} \quad (2.19)$$

K_y is a constant corresponding to an y percent rise in the rear face temperature (K=1.38 for V=0.5) and t_y is the time required to the temperature reach y of the maximum temperature.

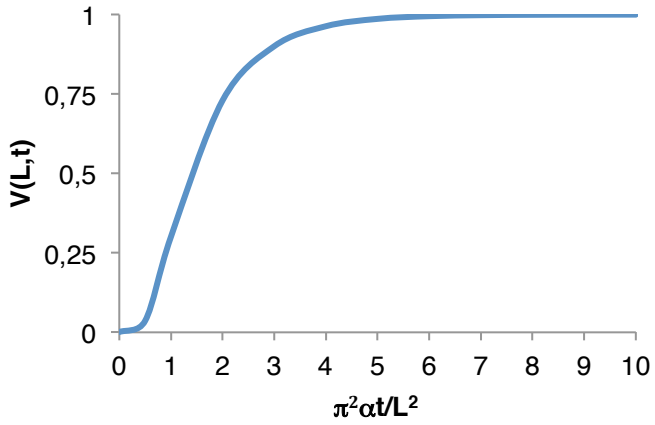

Figure 2.7: Graphic representation of equation 14: percent in temperature rise versus $\pi^2\alpha t/L^2$.

Equation 16 shows that is not necessary to know the amount of energy absorbed by the sample to determine thermal diffusivity. However, this quantity must be measured if specific heat and thermal conductivity are to be estimated [10].

Thermal diffusivity experiments are usually short and relatively simple. In contrast to the measurements used to access the thermal conductivity of a material, measuring thermal diffusivity involves the accurate recording of the temperature caused by a transient thermal disturbance in a thin layer of the sample. To measure thermal conductivity involves heat fluxes that are difficult to control and measure accurately. If the specific heat and density of the material are known thermal conductivity can be determined using equation 1. Due to the small variations in temperature in the sample during measurements, the measured property is related to an accurately known temperature this advantage allows the study of phase transitions via thermal diffusivity.

The transmission of photons (lattice vibrations) and free electrons are responsible for the heat flow within materials. If these “heat carriers” encounter defects in their path such as grain boundaries, solute atoms or pores they will be scattered which implies a reduction in thermal conductivity (and thermal diffusivity). It is expected that, when porous materials are tested for thermal diffusivity via laser flash technique, pores will affect the values measured. A decrease of thermal diffusivity with increasing porosity is usually observed [11].

2.2 Experimental Procedure

The WC-Cu cermets were performed via hot pressing changing the volume fraction of copper (Cu) (25, 50 and 75%). Based on the mold cavity volume (2.75cm^3), commercial powders of Cu (Alpha Aesar with grain size lower than 37μm with purity of 99.9%) and WC (Alpha Aesar and Sigma-Aldrich with grain size less than 2 μm with purities of 99.5%) were weighted inside a glovebox to avoid oxidation of the copper powder and mixed according to the respective volume fractions.

At the Portuguese company DIAPOR – Diamantes de Portugal, S.A [12] the WC-Cu powder mixture of each composition was submitted, in a first attempt to consolidate the materials, to turbula mixing during 30 min. After mixing the powders were weighted into 4 equal portions and feed to 4 graphite cavities dies with 10 mm of length, 55 mm of width and 5 mm of thickness to be consolidated. In the consolidations used to improve densification of the materials (green cells in Table 2.1), the powders mixtures were submitted to the same procedure but with mixing times of 90 min in the turbula. The hot pressing machine used in this work is an *Idea Vulcan 70 VP* HP, in this unit the powders are heated by induction phenomena and the pressure is unidirectionally applied. To avoid oxidation of the materials being consolidated nitrogen was purged into the atmosphere inside the hot pressing unit at the beginning of the consolidation process. The temperature of the consolidation process was controlled by a pyrometer coupled with the HP unit that reads the temperature at the surface of the graphite mold. The measured sintering temperature of the cermets ranges from 800 to 1150 °C. Thirteen cycles were tested to optimize the consolidation parameters by varying the pressure and temperature of the cycles as presented in Table 2.1. The parameters were adjusted in order to

achieve densities near to the theoretical ones. The *Idea Vulcan 70 VP* is water-cooled and the estimated cooling rate is the same for all the cycles and approximately equal to 2 °C/s.

Table 2.1: Temperature, pressure and time of the cycles tested for consolidate each cermet.
Cycle with two different isothermal steps: one at 875 °C and other at 975 °C.

	Composition		
Temperature (°C)	**75WC-25Cu**	**50WC-50Cu**	**25WC-75Cu**
800	34 MPa, 5 min	34 MPa, 5 min	34 MPa, 5 min
875*			27 MPa, 6 min
900	---	---	22 MPa, 5 min
925	---	34 MPa, 5 min	34 MPa, 5 min
975*			34 MPa, 2 min
1025	---	---	34 MPa, 5 min
1060	---	37 MPa, 5 min	---
1100	34 MPa, 5 min	34 MPa, 5 min	---
1150	44 MPa, 5 min	---	---
	47 MPa, 6 min	---	---

The theoretical density of the cermets can be easily calculated by:

$$\rho_{cermet} = f_{WC}\rho_{WC} + (1 - f_{WC})\rho_{Cu} \tag{2.20}$$

where ρ represents the density of the cermet (ρ_{cermet}), tungsten carbide (ρ_{WC}) and copper (ρ_{Cu}), respectively, and f_{WC} the volume fraction of the WC phase. The density of cermets was determined using Archimedes' method that is based on the water displacement method.

To access the internal microstructure of the WC-Cu cermets metallographic samples were made from the successfully consolidated cermets by cutting a small piece of the sample. The samples were hot mounted, polished up to a 0.5 μm silica oxide polishing suspension (OPS) and observed with SEM (Hitachi S2400 and JEOL JSM7001F) coupled with EDS (Bruker and Oxford 250 spectrometers) to characterize the cross section microstructure of the cermets. The diameter of the aggregates was determined by taking the overall height of 4 different aggregates and use the mean value as its maximum overall length (Feret's diameter).

The thermal diffusivity was carried out using *Laser Flash FL 5000* equipment, with polish cylindrical samples with 10 mm diameter and 4.5 mm height. Vickers hardness of the WC-Cu cermets was measured using a square diamond pyramid with loads of 2 and 20 N. The mean hardness of the cermets corresponds to the mean value resulting from 5 indentation tests for each sample. After measuring the hardness, the samples were observed with SEM in order to evaluate the cracks around the indentations. This observation allows a qualitative discussion of the adhesion between the copper matrix and the tungsten carbide particles.

2.3 References

[1] J. W. Christian, M. E. Fine, J. Friedel, J. J. Harwood, T. B. King, E. I. Salkovitz, A. Seeger, A. Sosin, F. F. Y. Wang, and F. R. S. P. B. Hirsch, *Treatise On Materials Science And Technology Volume 9: Ceramic Fabrication Processes*, vol. 9. Academic Press, Inc., 1976.

[2] S. and S. R. S. Kalpakjian, S. R. Schmid, and H. Musa, *MANUFACTURING ENGINEERING AND TECCHNOLOGY*, 6th ed. Prentice Hall, 2009.

[3] J. Goldstein, D. Newbury, D. Joy, C. Lyman, P. Echlin, E. Lifshin, J. Michae, and I. Charles, *Scanning Electron Microscopy and X-Ray Microanalysis*, Third. New York: Kluwer Academic/Plenum Publishers, 2003.

[4] "http://www.purdue.edu/rem/rs/sem.htm," 2011. [Online]. Available: http://www.purdue.edu/rem/rs/sem.htm.

[5] Amelinckx, Hall, Joy, Snyder, Telle, Petzow, Keliher, Skelly, Gallagher, and Gerson, *Materials Science and Technology: A Comprehensive Treatment (Book 1)*. Wiley-VCH, 2006.

[6] Z. H. Stachurski, *Mechanical behavior of materials*, vol. 12, no. 3. 2009.

[7] Gordon England, "Vickers indenter," 2015. [Online]. Available: http://www.gordonengland.co.uk/hardness/vickers.gif. [Accessed: 02-Jun-2015].

[8] D. D. Elton N. Kaufmann, Reza Abbashian, Peter A. Barnes, Andrew B. Bocarsly, Chia-Ling Chien, *Characterization of Materials, 2 volume set*. John Wiley & Sons, Inc., 2003.

[9] I. Standard, "ISO 6507-1: Metallic materials-Vickers hardness test," vol. 1997, 1997.

[10] W. J. Parker, R. J. Jenkins, C. P. Butler, and G. L. Abbott, "Flash method of determining thermal diffusivity, heat capacity, and thermal conductivity," *J. Appl. Phys.*, vol. 32, no. 9, pp. 1679–1684, 1961.

[11] T. Takahashi and T. Kikuchi, "Porosity dependence on thermal diffusivity and thermal conductivity of lithium oxide Li2O from 200 to 900°C," *J. Nucl. Mater.*, vol. 91, no. 1, pp. 93–102, 1980.

[12] "DIAPOR." [Online]. Available: http://www.diapor.pt. [Accessed: 21-Oct-2015].

3 Results and Discussion

The results presented in this chapter are divided according to compositions of the cermets. Three compositions were produced via hot pressing and the production cycles were optimized to obtain materials with high density. The following subsections described the microstructural features, Vickers hardness and thermal diffusivity of each composition cermet.

3.1 75WC-25Cu Cermet

3.1.1 Hot Pressing Cycles

Consolidation of the 75WC-25Cu cermets was performed under four hot pressing different cycles as shown in Table 3.1. The temperature and pressure of the cycles ranged from 800 to 1150 °C and 34 to 47 MPa, respectively. The first attempt to consolidate the materials, 75WC-25Cu$_{cycle1}$, was performed below the melting temperature of copper (1083 °C [1]) to avoid the formation of a liquid phase that could cause distortion on the materials produced while relying on the high ductility of solid copper at high temperature [2]. However, due to the low temperature of the cycle, the materials were not consolidated and presented granulates weakly bounded (Figure 3.1).

Figure 3.1: Material resulting from consolidation under 75WC-25Cu$_{cycle1}$ conditions.

In fact, conventional sintering of WC cermets is based on the formation of a liquid phase [3], [4]. WC and molten copper present good wetting characteristics resulting in a good interfacial bond between WC particles and the Cu matrix [5]. In this line of reasoning the next cycles were carried out above the melting temperature of copper and also at increased pressure, resulting in the production of dense materials (75WC-25Cu$_{cycle2}$ to 75WC-25Cu$_{cycle4}$, Table 3.1). The higher pressure is expected to have two effects; firstly increase the compaction of the solid particles and secondly force the liquid copper to between the particles eliminating pores.

Table 3.1: Temperature, pressure and holding time of the cycles tested to produce the 75WC-25Cu cermets and the respective densification obtained.

Cycle/Cermet	Temperature (°C)	Pressure (MPa)	Holding time (min)	Densification (%)	Consolidation
75WC-25Cu$_{cycle1}$	800	34	5	---	✖
75WC-25Cu$_{cycle2}$	1100	34	5	75	✔
75WC-25Cu$_{cycle3}$	1150	44	5	88	✔
75WC-25Cu$_{cycle4}$	1150	47	6	95	✔

Figure 3.2 shows the temperature vs. time of each cycle tested for the 75WC-25Cu cermets. Since the pyrometer reads the temperature at the surface of the graphite mold, such temperature is not exactly

the same at the materials being consolidated. Therefore, the linear cooling rate represented is an approximation of the real cooling rate of the materials. The maximum pressure in 75WC-25Cu$_{cycle2}$, 75WC-25Cu$_{cycle3}$ and 75WC-25Cu$_{cycle4}$ was directly applied after the first step (900 °C) and kept until the end of the cycle, while in the case of 75WC-25Cu$_{cycle1}$ the maximum pressure was applied only when the cycle reached 800 °C and was maintained until the end of the cycle.

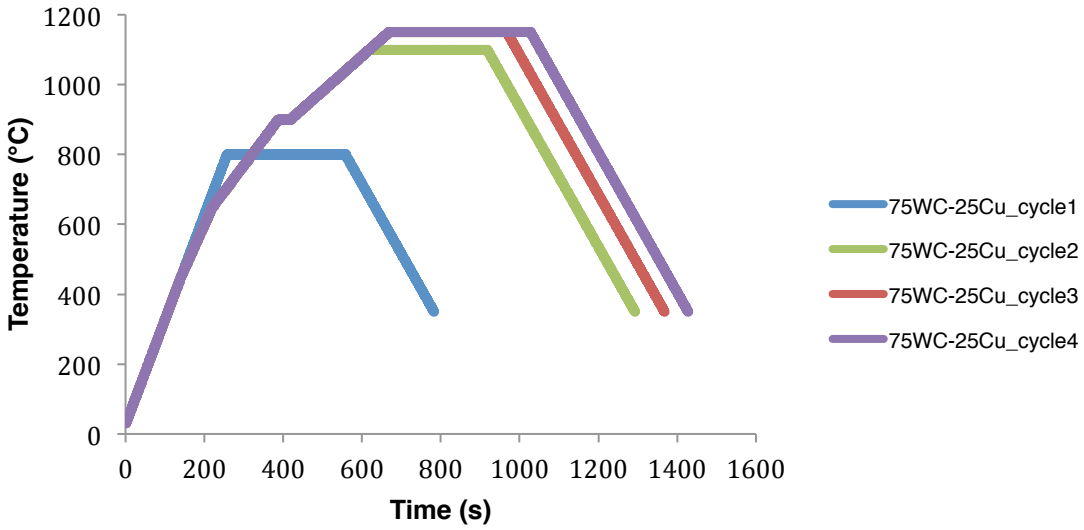

Figure 3.2: Temperature vs. time of the four cycles tested for the 75WC-25Cu cermets.

3.1.2 Microstructural characterization

Figure 3.3 (a) and (b) shows the microstructure resulting from the 75WC-25Cu$_{cycle2}$ conditions (Table 3.1). The formation of a liquid phase is expected to have lead to a rapid initial densification due to the capillary force exerted by the wetting molten copper on the tungsten carbide particles [2]. However, the consolidated materials presented residual porosity (Figure 3.3 (a), Table 3.1). The distribution of WC in the Cu matrix is homogeneous with the presence of some WC aggregates with a larger diameter than that of the starting powders, which indicates particle coalescence during the consolidation process (Figure 3.3 (b)).

To promote a higher densification of the materials, pressure and temperature were increase to 44 MPa and 1150 ^{o}C, respectively. The microstructure of the cermet resulting from the consolidation according to 75WC-25Cu$_{cycle3}$ is shown in Figure 3.3 (c) and (d). Densification increased about 13% according to the Archimedes' method (Table 3.1). When the liquid (Cu) is formed it tends to fill the smallest pores (due to capillarity effects) in order to minimize the total energy of the system, this behavior results in the presence of larger pores at the sites occupied by the copper particles prior melting [6]. Large WC aggregates were observed in this sample (Figure 3.3 (d)). The balance between the surface energy of the solid, surface tension of the liquid and liquid-solid interfacial energy dictates the wettability of the solid phase by the liquid. In cases were incomplete wetting occurs (wetting (or contact) angles greater than 0º but less than 90º) coalescence of solid grains occurs [7]. The contact

angle of liquid copper on WC with a particle size less then 2 μm at 1100 ºC was reported to be approximately 30º [5]. This suggests that incomplete wetting occurs and the requirements of surface-energy relationships led these small grains to coalesced and form large clusters [8]. In addition, application of an higher pressure promotes particle sliding and rearrangement into a denser configuration [9].

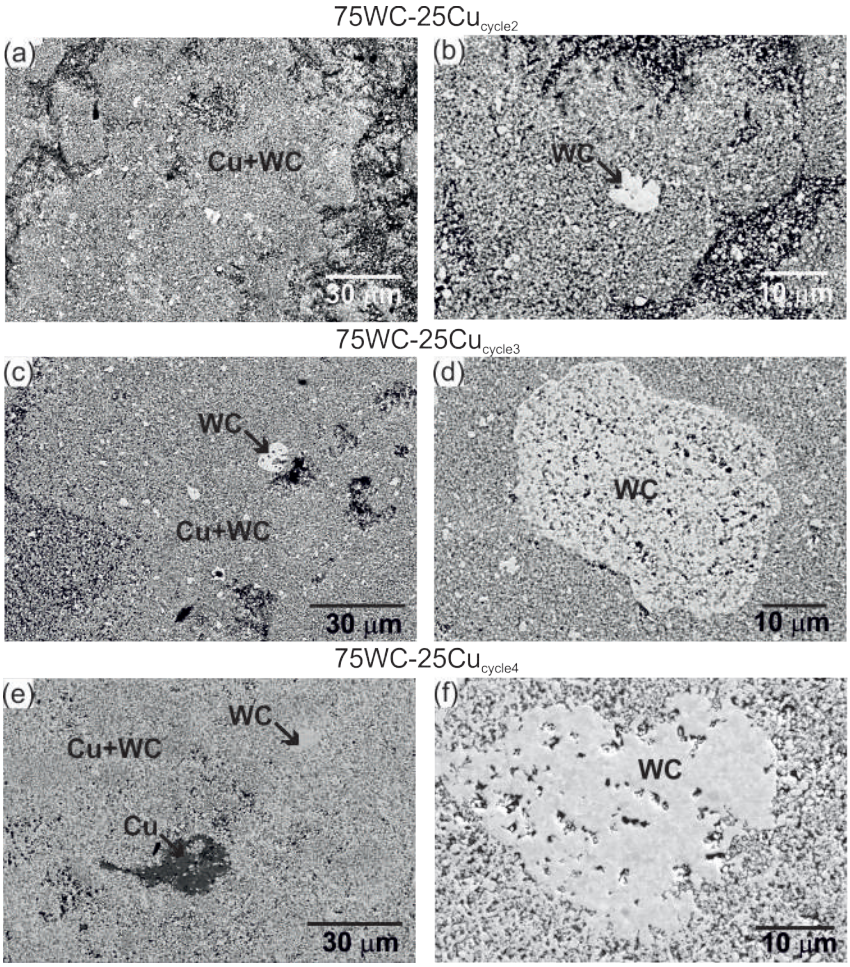

Figure 3.3: BSE images revealing the microstructures resulting from the consolidation under conditions of 75WC-25Cu$_{cycle2}$ ((a) and (b)), 75WC-25Cu$_{cycle3}$ ((c) and (d)) and 75WC-25Cu$_{cycle4}$ ((e) and (f)).

A third attempt to raise the densification of the material was conducted under 75WC-25Cu$_{cycle4}$ conditions. Figure 3.3 (e) shows the presence of copper patches in the microstructure of the materials consolidated in this cycle. The high pressure applied (47 MPa) during 75WC-25Cu$_{cycle4}$ may be responsible for the formation of the copper patches by forcing the liquid copper to fill existing large pores. EDS analyses identified traces of Zn and O in the copper-regions (see black arrows in Figure 3.4).

Similarly to the 75WC-25Cu$_{cycle2}$ and 75WC-25Cu$_{cycle3}$ samples, the microstructure of the 75WC-25Cu$_{cycle4}$ sample evidenced the coalescence of WC particles with average size of 37 ± 8 μm (Figure 3.3 (f)) and more compact than those observed in the previous samples, as the applied pressure in cycle 4 was higher (47 MPa). Such particles in 75WC-25Cu$_{cycle4}$ samples possessed a mosaic structure typical of polycrystalline aggregates (Figure 3.5).

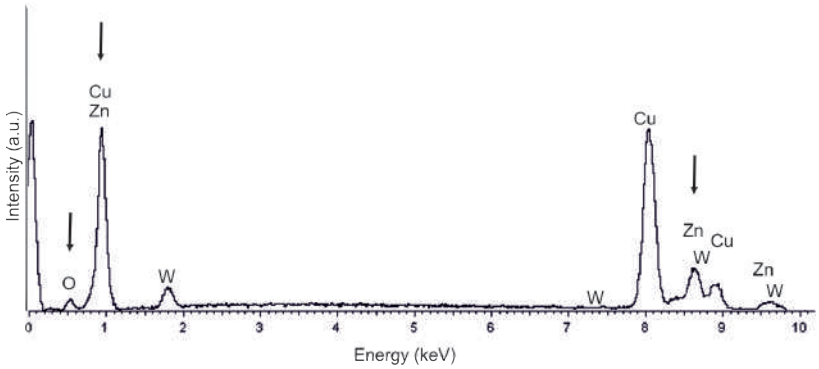

Figure 3.4: EDS spectrum of the copper patches present in the 75WC-25Cu$_{cycle4}$ cermets.

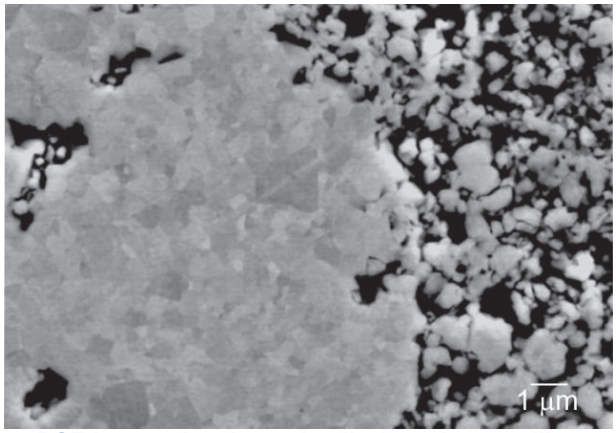

Figure 3.5: BSE image showing a detail of a polycrystalline aggregate.

3.1.3 Vickers Hardness

Vickers Hardness measurements obtained using loads of 2 (HV0.2) and 20 N (HV2) were performed on the cermets consolidated under the 75WC-25Cu$_{cycle2}$, 75WC-25Cu$_{cycle3}$ and 75WC-25Cu$_{cycle4}$ condition and are shown in Table 3.2. The $\sigma_{0.2}$ and σ_2 parameters represent the standard deviation associated to the HV0.2 and HV2 measurements, respectively. Due to the small diameter of the WC particles a small load (1.961N) is required to locally observe the behavior of the WC/Cu interface. On the other hand, the high load tests gave qualitative information about the general behavior of the WC + Cu matrix, i.e., if the material deforms without formation of cracks.

Table 3.2: Mean HV0.2 and HV2 values of the 75WC-Cu cermets produced and the respective standard deviation of the measurements.

Cycle/Cermet	HV0.2 (MPa)	$s_{0.2}$ (MPa)	HV2 (MPa)	s_2 (MPa)
75WC-25Cu$_{cycle2}$	625	122	505	133
75WC-25Cu$_{cycle3}$	567	62	520	49
75WC-25Cu$_{cycle4}$	1170	201	463	225

Despite the difference of 13% in densification of the samples produced under 75WC-25Cu$_{cycle2}$ and 75WC-25Cu$_{cycle3}$ condition the HV0.2 and HV2 values for those samples are in the same range.

Sample 75WC-25Cu$_{cycle4}$ evidenced the higher hardness values, which seems to be related with the high densification (95%) achieved for this cycle. The samples' porosity reduces the volume resistant to mechanical stresses and concentrate stresses, decreasing the hardness of ceramics [10]. Figure 3.6 shows a detail of the Vickers indentation resulting from a load of 20 N in the 75WC-25Cu$_{cycle4}$ cermets, where it can be seen that the high load caused the intergranular fracture of the WC grains but no decohesion between the WC grains and the copper matrix. For the indentation using a load of 2 N neither fracture nor decohesion were observed. Since the HV2 indenter covers a larger area of test, the size of the indenter may also affect the values measured because the probability of finding a defect (pores) increases with the area tested.

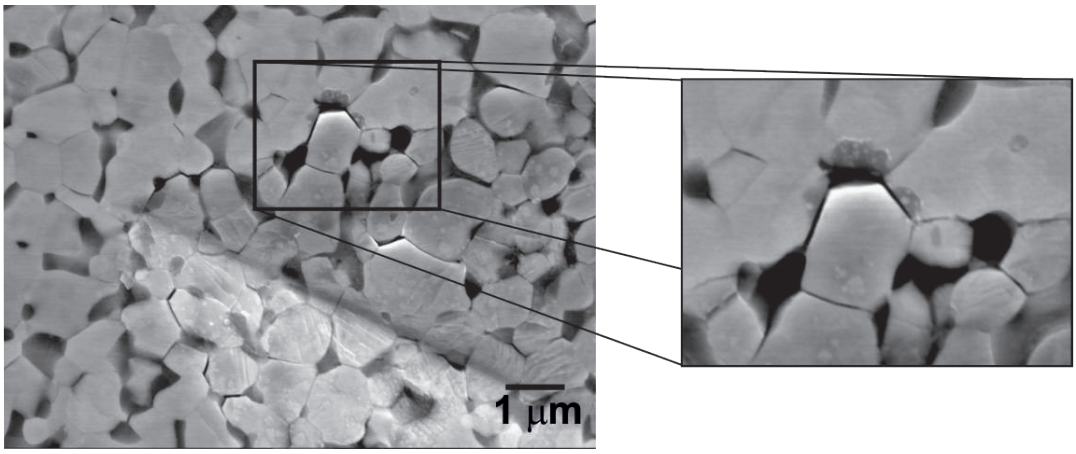

Figure 3.6: SE image showing a detail of a Vickers indentation resulting from an applied load of 19.614 N in the cermets produced according to 75WC-25Cu$_{cycle4}$.

3.1.4 Thermal diffusivity

The temperature dependence of thermal diffusivity of the sample with higher densification (75WC-25Cu$_{cycle4}$) was determined and compared to the thermal diffusivity of pure Cu [1], pure W [11] and pure WC [12] as shown in Figure 3.7. Since the cermet presents a high content of WC, the thermal behavior of the materials is close to the one of pure WC. The thermal dependence of thermal diffusivity of the 75WC-25Cu$_{cycle4}$ samples seems to follow the behavior of Cu and WC, i.e., it decreases with increasing temperature.

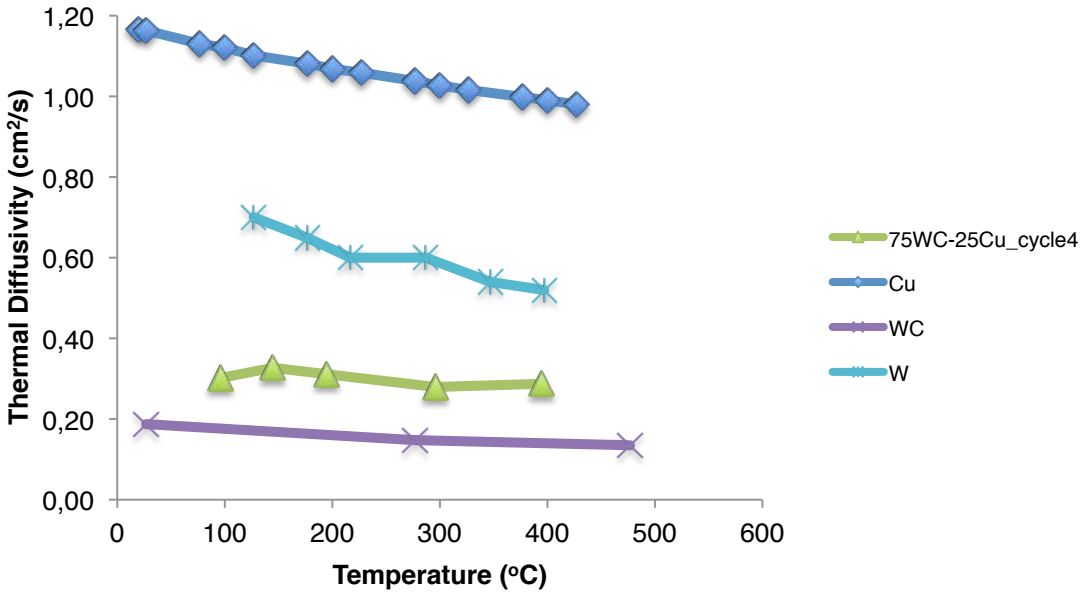

Figure 3.7: Temperature dependence of thermal diffusivity of Cu, WC, 75WC-25Cu$_{cycle3}$ and 75WC-25Cu$_{cycle4}$ cermets.

3.2 50WC-50Cu Cermet

3.2.1 Hot Pressing Cycles

To produce 50WC-50Cu cermets four different hot pressing cycles were tested. The maximum temperature, pressure and holding time of the cycles, as well as the densifications obtained, are presented in Table 3.3.

Table 3.3: Temperature, pressure and holding time of the hot pressing cycles tested to produce the 50WC-50Cu cermets and the respective densification obtained.

Cycle/Cermet	Temperature (°C)	Pressure (MPa)	Holding time (min)	Densification (%)	Consolidation
50WC-50Cu$_{cycle1}$	800	34	5	---	✖
50WC-50Cu$_{cycle2}$	925	34	5	---	✖
50WC-50Cu$_{cycle3}$	1100	34	5	73	✔
50WC-50Cu$_{cycle4}$	1060	37	5	92	✔

Since these materials present a higher fraction of Cu, two solid-state sintering attempts have been carried out due to anticipated difficulties associated with liquid phase sintering, such as distortion for high volume fraction of liquid (>30%) [2]. Two temperatures, below the melting temperature of copper, were tested in cycles 50WC-50Cu$_{cycle1}$ and 50WC-50Cu$_{cycle2}$. Nonetheless, the temperature-holding time of both cycles were insufficient to produce bulk materials as shown in Figure 3.8 for sample 50WC-50Cu$_{cycle1}$.

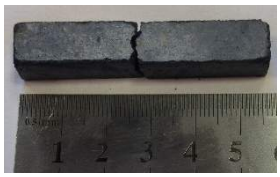

Figure 3.8: Materials consolidated with 50WC-50Cu$_{cycle1}$ conditions.

Two additional cycles of liquid phase sintering have been conducted (50WC-50Cu$_{cycle3}$ and 50WC-50Cu$_{cycle4}$) It must be pointed out that although the nominal temperature of 50WC-50Cu$_{cycle4}$ was lower than the melting temperature of copper, liquid was formed during the consolidation cycle. This could have resulted from the imprecise temperature measurement at the mold wall and/or heterogeneous temperature distribution and/or existence of residual impurities that reduced the melting temperature of copper. The phase diagram of the system Cu-O presents an eutectic reaction between Cu and Cu_2O at 1066 ^{o}C as shown in Figure 3.9. EDS confirmed the presence of oxygen and zinc in the copper islands in the microstructures of the 50WC-50Cu$_{cycle4}$ samples (Figure 3.10).

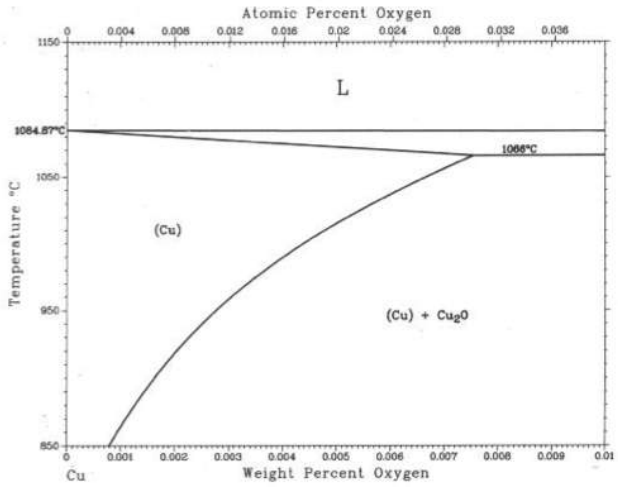

Figure 3.9: Solubility of O in Cu [13].

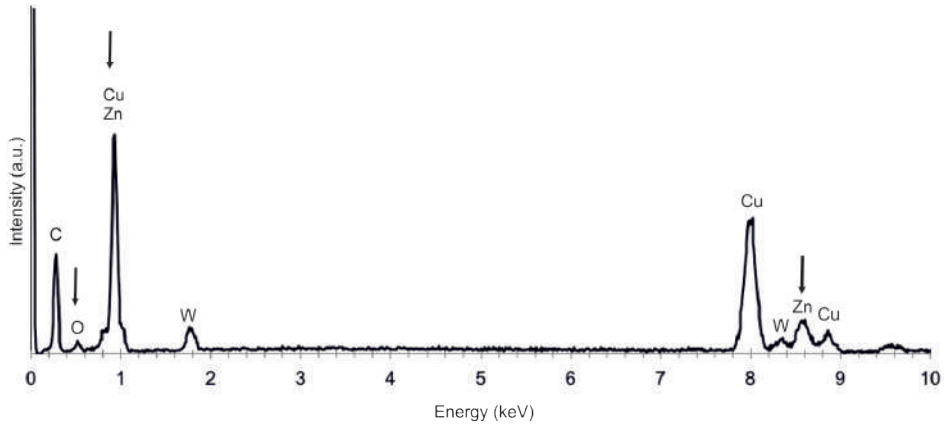

Figure 3.10: EDS spectrum of the copper patches present in the 50WC-50Cu$_{cycle4}$ cermets.

Comparing the densification obtained in the two cycles, 73% for 50WC-50Cu$_{cycle3}$ and 92% for 50WC-50Cu$_{cycle4}$ it is clear that pressure was key in promoting densification for this temperature range. The densification and shrinkage increase as the amount of liquid increases [14], in addition, the external pressure aids densification causing pore collapse [15]. The liquid phase lubricates particle sliding induced by the external pressure and consequently pores and inhomogeneous regions are eliminated [2]. During this rearrangement stage, the rate of densification increases as the capillary force increases in the material [9].

Figure 3.11 shows the time dependence of temperature of the 50WC-50Cu cycles. The cooling rates determined in the cycles are approximately equal to the ones estimated for the cycles 75WC-25Cu (2 ^{o}C/s). The pressure applied during the cycles follows the same rules explained for the 75WC-25Cu, i.e., the maximum pressure is applied after the first isothermal step and is kept until the cycles' end. In the case of 50WC-50Cu$_{cycle1}$ the maximum temperature was applied when maximum temperature was reached.

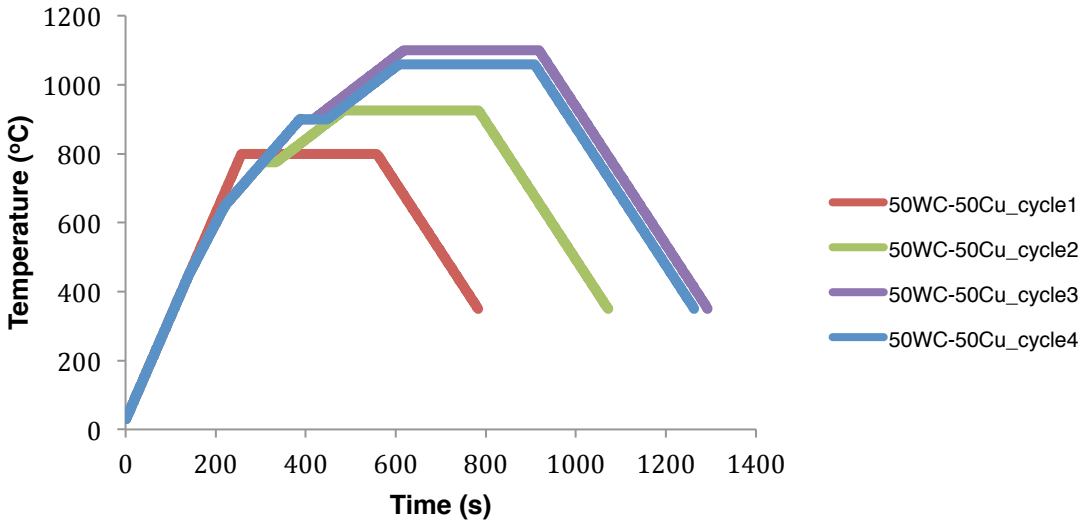

Figure 3.11: Variation of temperature with time for the cycles used to consolidate 50WC-50Cu cermets.

3.2.2 Microstructural Characterization

The materials consolidated under 50WC-50Cu$_{cycle3}$ conditions showed high porosity and the presence of copper-rich patches as shown in Figure 3.12 (a). Small WC aggregates similar to the ones found in the 75WC-25Cu$_{cycle2}$ materials were observed (Figure 3.12 (b)), however their presence was less frequent.

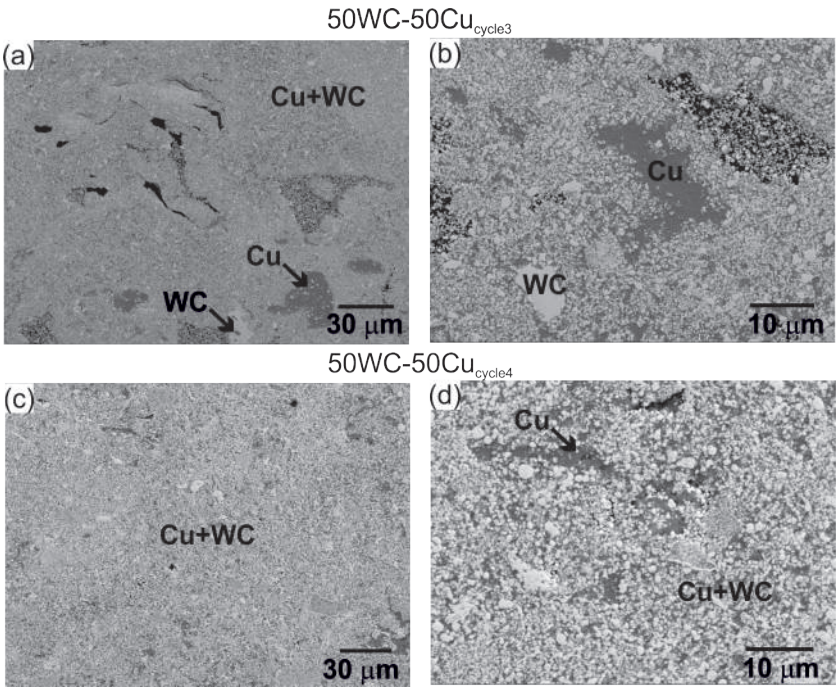

Figure 3.12: BSE images showing the microstructure of the consolidated materials according to 50WC-50Cu$_{cycle3}$ and 50WC-50Cu$_{cycle4}$.

In Figure 3.12 (a) and (b) the porosity reduction is evident and corresponds to an increase of 19% in densification from 50WC-50Cu_{cycle3} to 50WC-50Cu_{cycle4} samples. Another microstructural feature of the latter material was the reduction of number and size of the copper patches (compare Figure 3.12 (b) and (d)). The powders used to produce 50WC-50Cu_{cycle3} samples where submitted to turbula mixing for 30 minutes, while the ones used to produce the 50WC-50Cu_{cycle4} samples where mixed for 90 minutes. The larger mixing time may have promoted homogenization of the final microstructure of the cermets.

Figure 3.13 shows the formation of WC aggregates (with average size of 21 ± 6 μm) found in samples consolidated according to 50WC-50Cu_{cycle4} conditions. The overall faceted shape and the grain contrast in these slab-like aggregates (Figure 3.13 (a)) suggests aggregation along preferred orientations and coalescence of the WC particles [16]. It seems that, as it occurs in the WC-Co system, in WC submicron sized powders there is a preferred grain boundary orientation between WC grains [17] which makes grain growth by coalescence easier. EDS analyses performed on the WC aggregates did not reveal the presence of elements other than C, W and Cu, which could have changed the surface energy of the WC/WC and WC/Cu interfaces leading to the agglomeration of the WC particles (Figure 3.14).

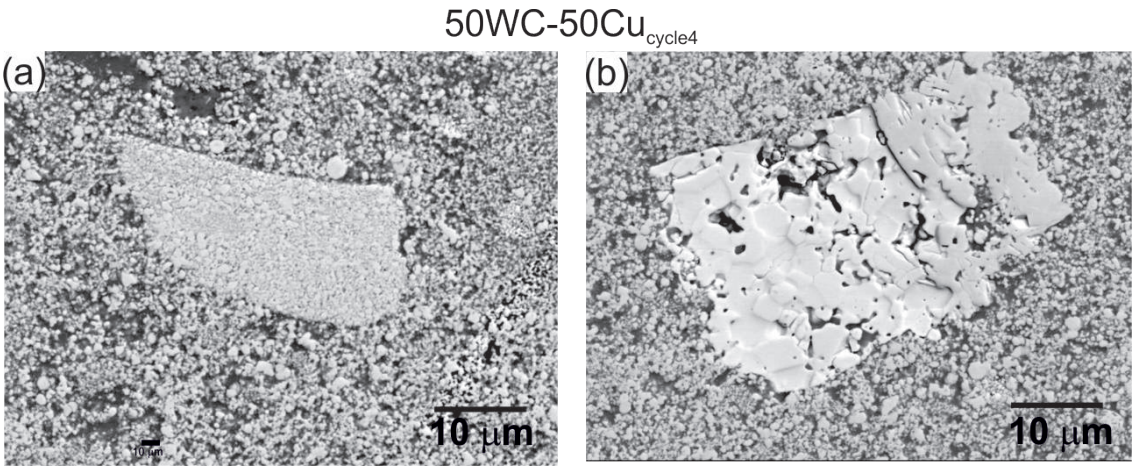

Figure 3.13: BSE showing WC aggregates formation in sample 50WC-50Cu_{cycle4}. (a) Clusters of small WC grains forming larger WC aggregates and (b) slab-like aggregates.

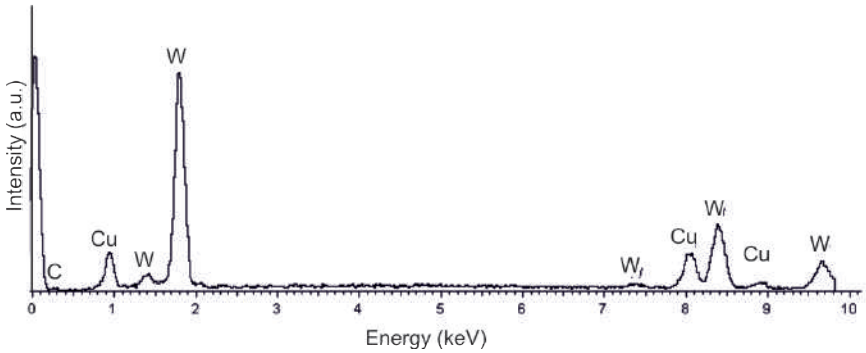

Figure 3.14: EDS spectrum of the WC aggregate.

3.2.3 Vickers Hardness

The HV0.2 and HV2 measurements are present in Table 3.4. The increase of Cu content (and reduction of WC) causes the hardness to decrease in comparison to the 75WC-25Cu cermets. As densification increases the hardness of the samples increases as well, this effect is more visible for the HV0.2 measurements.

Table 3.4: Mean HV0.2 and HV2 values of the B cermets and the respective standard deviation.

Cycle/Cermet	HV0.2 (MPa)	$\sigma_{0.2}$ (MPa)	HV2 (MPa)	σ_2 (MPa)
50WC-50Cu$_{cycle3}$	453	53	377	30
50WC-50Cu$_{cycle4}$	676	46	395	50

The difference between the mean values of HV0.2 and HV2 is due to the non-homogeneity of these materials. Figure 3.15 (b) shows a detail of a HV2 indentation where a crack is propagating through the copper between WC grains (see black arrows). The higher content of copper (in contrast with the 75WC-25Cu composition) increases the toughness of the cermets, which promotes deformation accommodation rather than fracture caused by the load applied. No cracks were observed around the indentations caused by the load of 2 N (HV0.2).

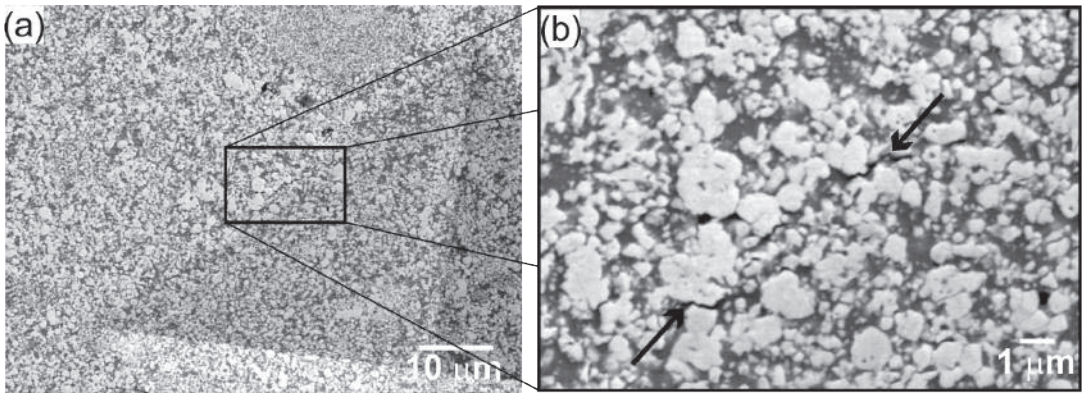

Figure 3.15: SE images showing the (a) HV2 indentations of the 50WC-50Cu$_{cycle4}$ cermets. In (b) is shown a detail of the HV2 indentation. The arrows in (b) indicate intergranular fracture.

3.2.4 Thermal Diffusivity

Despite the higher content of copper, the 50WC-50Cu$_{cycle3}$ cermets present a lower thermal diffusivity than any of the 75WC-25Cu cermets, which can be justified by the higher porosity. The 50WC-50Cu$_{cycle3}$ cermets present the lowest relative density (73%) as well the lowest values of thermal diffusivity of all the materials consolidated. In fact the thermal diffusivity of the cermets 50WC-50Cu$_{cycle3}$ present lower values than those of pure WC (Figure 3.16). In contrast the cermets 50WC-50Cu$_{cycle4}$ present higher thermal diffusivity than the 75WC-25Cu cermets due to the higher content of copper and high densification (92%).

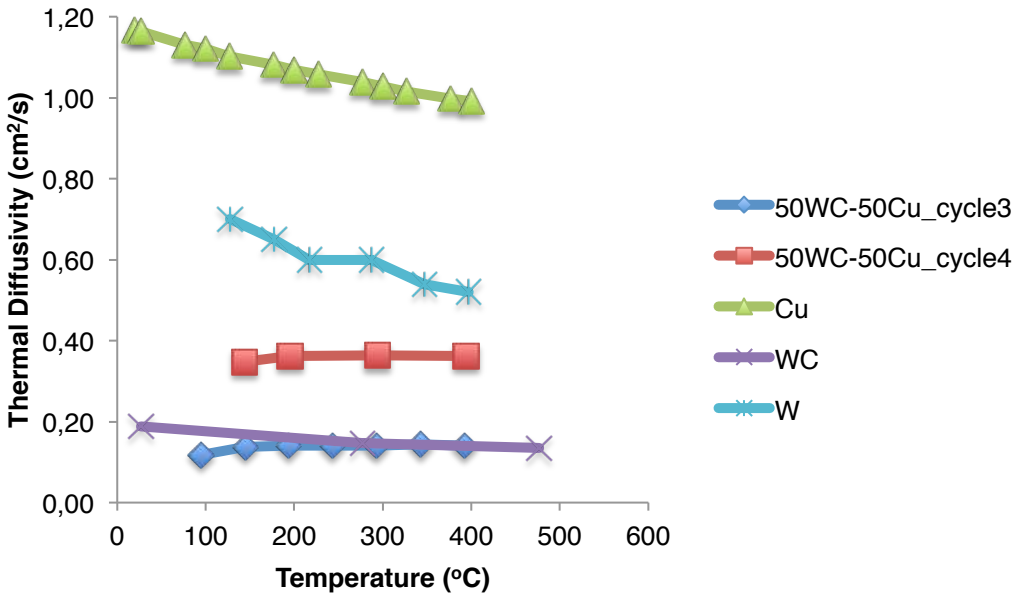

Figure 3.16: Thermal diffusivity of the 50WC-50$_{cycle3}$ and 50WC-50Cu$_{cycle4}$ cermets as function of temperature.

3.3 25WC-75Cu Cermet

3.3.1 Hot Pressing Cycles

Since the 25WC-75Cu cermets present the highest content of copper, several consolidation attempts through solid-state sintering were carried out. The conditions of the cycles used are presented in Table 3.5, the cycle designation is ordered by temperature and not by the order of which they were tested. The temperature, pressure and holding time of the first cycle tested (25WC-75Cu_{cycle1}) were the same as for 75WC-25Cu_{cycle1} and 50WC-50Cu_{cycle1}. Despite the difference in copper this common cycle did not promote effective consolidation of any of the materials. In the next cycles tested (25WC-75Cu_{cycle4} and 25WC-75Cu_{cycle5}) pressure and holding time were maintained at 34MPa and 5 min, respectively and only temperature was increased. The materials resulting from 25WC-75Cu_{cycle3} and 25WC-75Cu_{cycle5} are shown in Figure 3.17. The 25WC-75Cu_{cycle3} materials did not sinter suitably and resulted in a powder compact with very low mechanical strength. Consolidation according to 25WC-75Cu_{cycle5} produced massive materials, however the final composition of the cermet was not 25WC-75Cu (vol.%) due to copper extravasation from the mold (see black arrow in Figure 3.17 (b)) caused by the high pressure (34 MPa) applied.

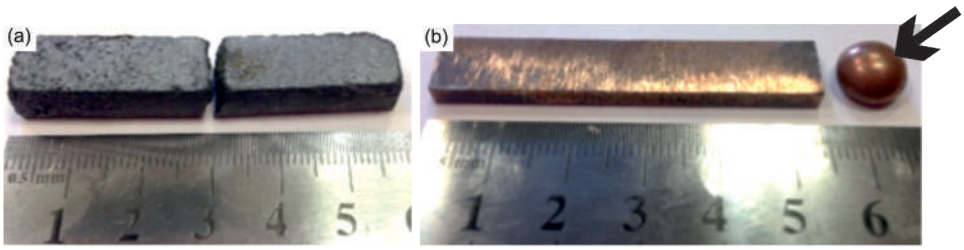

Figure 3.17: Materials consolidated according to cycle (a) 25WC-75Cu_{cycle3} and (b) 25WC-75Cu_{cycle5}.

Once more the maximum temperature of the cycle 25WC-75Cu_{cycle5} is lower than the melting temperature of copper but a liquid phase formed. This phenomenon may be explained by the same reasons mentioned in the discussion of the 50WC-50Cu_{cycle4} material. The 25WC-75Cu_{cycle4} conditions are characterized by two principal isothermal steps: one at 875 ^{o}C under 27 MPa during 6 min and other at 975 ^{o}C under 34 MPa during 2 min as shown in Figure 3.18. Since higher temperatures of sintering require lower holding times to achieve high densification through solid state sintering of copper powders [18], consolidation under 25WC-75Cu_{cycle4} conditions was expected to achieve better results than both 25WC-75Cu_{cycle1} and 25WC-75Cu_{cycle3}.

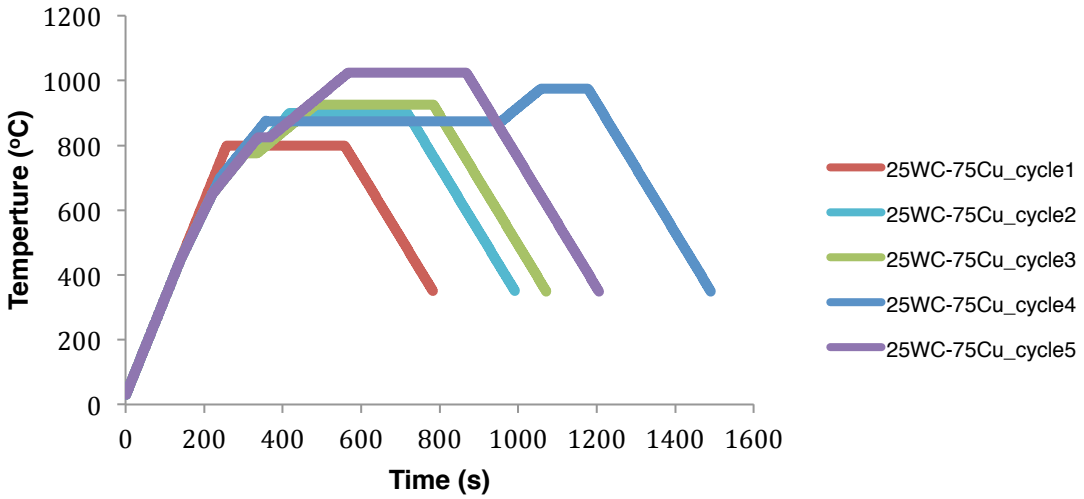

Figure 3.18: Temperature vs. time of the 25WC-75Cu cycles.

The 25WC-75Cu$_{cycle4}$ conditions were able to produce consolidated cermets, however due to the high pressure applied liquid copper escaped the mold, resulting in cermets with a final composition different from the one desired, as with 25WC-75Cu$_{cycle5}$.

Table 3.5: Temperature, pressure and holding time of the cycles tested to consolidate the 25WC-75Cu cermets.

Cycle/Cermet	Temperature (°C)	Pressure (MPa)	Holding time (min)	Densification (%)	Consolidation
25WC-75Cu$_{cycle1}$	800	34	5	---	✖
25WC-75Cu$_{cycle2}$	900	22	5	91	✔
25WC-75Cu$_{cycle3}$	925	34	5	---	✖
25WC-75Cu$_{cycle4}$	875 + 975	27 + 34	6 + 2	---	✖
25WC-75Cu$_{cycle5}$	1025	34	5	---	✖

To avoid liquid copper extravasation the pressure of the cycle should be controlled. In that sense the load and the mode how load was applied during 25WC-75Cu$_{cycle2}$ differed from all the cycles tested. Until then the pressure was instantaneously applied to the powder mixture at the final of the first step in the temperature vs. time curve (except for cycles 75WC-25Cu$_{cycle1}$, 50WC-50Cu$_{cycle1}$ and 25WC-75Cu$_{cycle1}$) and kept until the cycle's end. In the 25WC-75Cu$_{cycle2}$ the pressure was proportionally increased with increasing temperature, this allowed to control the copper extravasation by instantaneously stopping the increase in pressure when liquid copper escaped the mold.

The consolidation temperature of the 25WC-75Cu$_{cycle2}$ is lower than the melting temperature of copper, however liquid Cu is formed therefore the control of pressure is required. For the tested conditions 22 MPa is the maximum pressure that can be applied without Cu extravasation. The resulting materials presented a densification of 91%.

3.3.2 Microstructural Characterization

Figure 3.19 shows the microstructure of the cermets produced according to consolidation conditions of 25WC-75Cu$_{cycle2}$. A skeleton of interconnected copper pools surrounds Cu + WC composite regions (Figure 3.19 (a)). In contrast to the denser 75WC-25Cu and 50WC-50Cu cermets, in these samples no large WC aggregates were found. The starting WC powders have a grain size less than 2 μm and no grain growth was observed (Figure 3.19 (c)). Due to the large volume fraction of liquid phase a greater penetration of copper between the WC particles was possible as shown in Figure 3.19 (c). No oxides were detected by EDS (Figure 3.20).

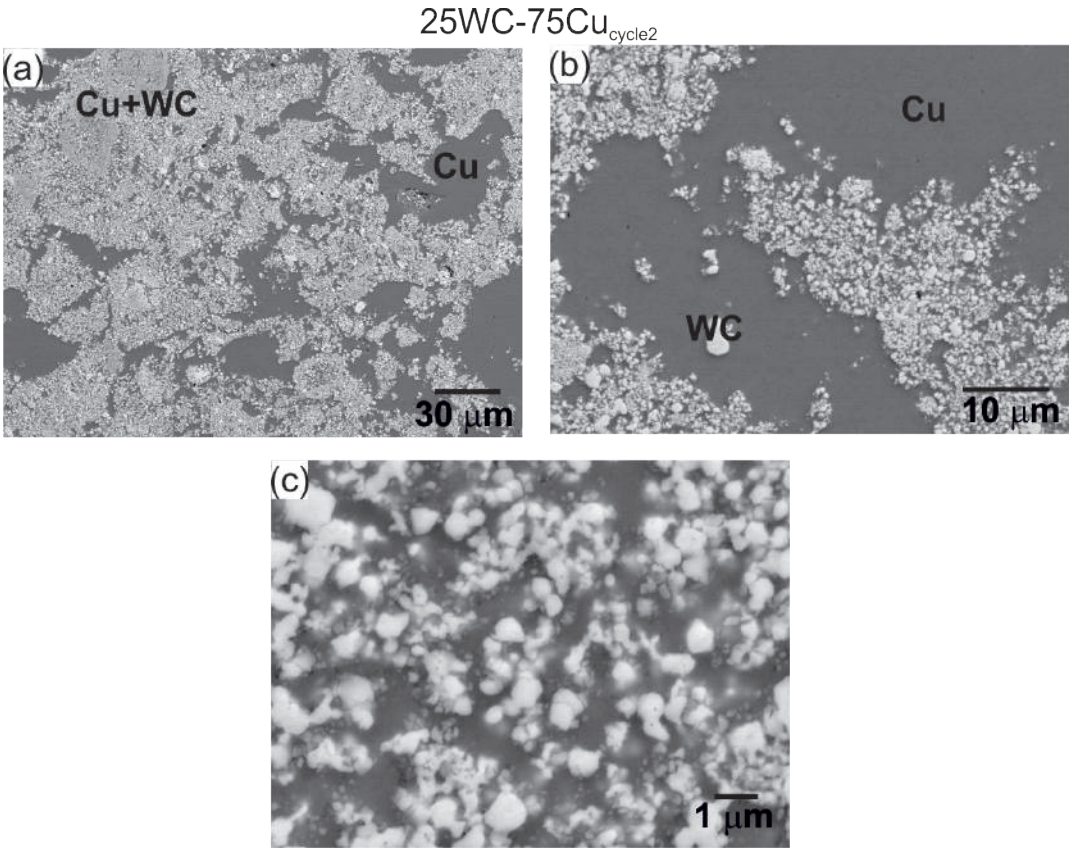

Figure 3.19: BSE images revealing the microstructure of the 25WC-75Cu$_{cycle2}$ cermets; (a) low amplification revealing the copper islands and the WC particles, which are shown in more detail in (b) and (c), respectively.

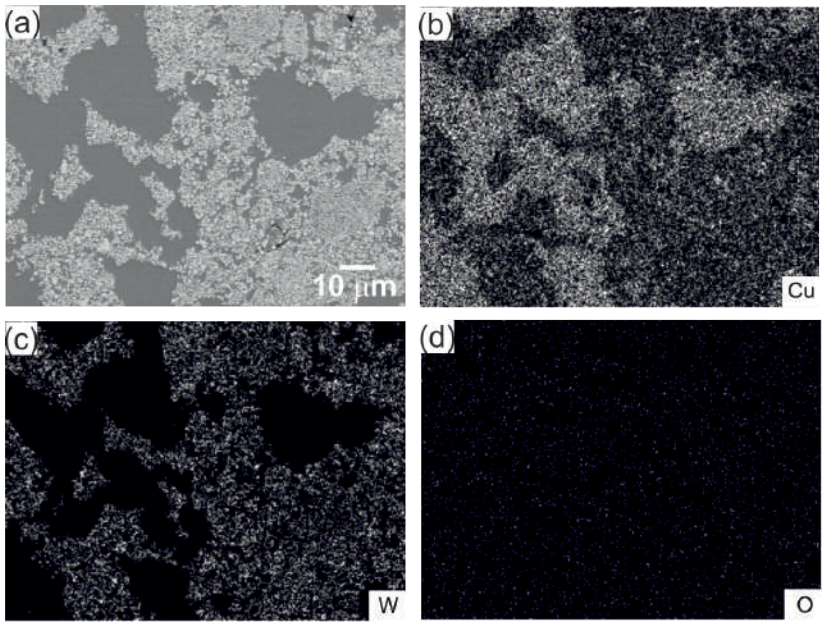

Figure 3.20: (a) Microstructure of the 25WC-75Cu$_{cycle2}$ cermets and the EDS maps of (b) Cu, (c) W and (d) O elements. Corresponding X-ray maps for Cu–Kα_1 , W– Mα_1 and O– Kα_1.

Since liquid copper formed below the melting temperature of copper, the copper patches were analysed in order to check contaminations that may have caused the decrease in the melting temperature of copper. The resulting EDS spectrum is shown in Figure 3.21 and no traces of another elements were detected. It must be pointed that very small concentrations of oxygen may cause a decrease in the melting temperature of copper (Figure 3.9) and that the EDS detector can only detect elements with a concentration higher than 1 wt.% [19]. This limit may not be enough to detect the small quantity of oxygen (or other impurities) present in samples that may have caused the reduction in the melting temperature of copper. Nevertheless, a large error associated with the pyrometer and the real temperature inside the mold may exist.

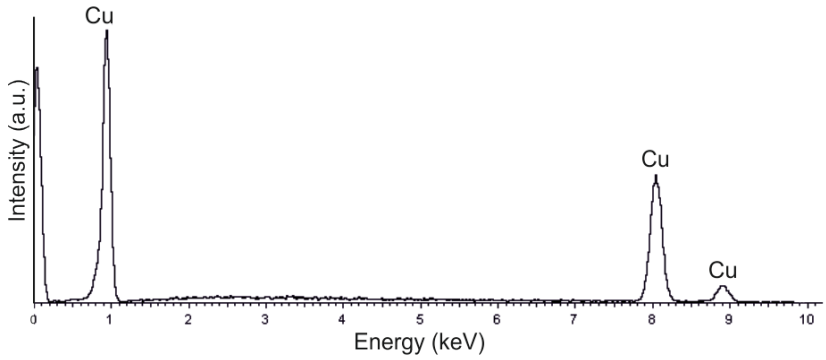

Figure 3.21: EDS spectrum of the copper islands presents in the 25WC-75Cu$_{cycle2}$ cermets.

3.3.3 Vickers Hardness

The Vickers hardness values of the cermets produced according to 25WC-75Cu$_{cycle2}$ are shown in Table 3.6. As expected the higher volume fraction of Cu yields lower hardness of the materials

Table 3.6: Mean Hv0.2 and HV2 values of the 25WC-75Cu$_{cycle2}$ cermets and the respective standard deviation.

Cycle/Cermet	HV0.2 (MPa)	$\sigma_{0.2}$ (MPa)	HV2 (MPa)	σ_2 (MPa)
25WC-75Cu$_{cycle2}$	262	47	139	20

The micrographs of the high load indentations (HV2) show the plastic deformation occurred in copper matrix after the indentation test (Figure 3.22). Some linear surfaces traces, probably twins or slip bands, were also observed around the indentation [20] (see black arrows in Figure 3.22). No decohesion at the interfaces between the WC particles and the copper matrix was observed. Since the 25WC-75Cu$_{cycle2}$ material did not have aggregates and consequently presented a low number of particle-particle contacts, the copper interlayers caused a decrease of hardness [21].

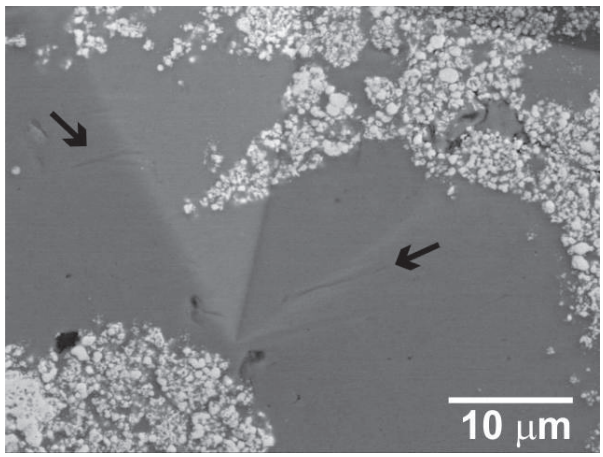

Figure 3.22: Micrograph showing a detail of the HV2 indentation of a 25WC-75Cu$_{cycle2}$ sample.

3.3.4 Thermal diffusivity

The variation of thermal diffusivity with temperature of the 25WC-75Cu$_{cycle2}$ cermets is presented in Figure 3.23. Comparing the temperature dependence of thermal diffusivity of cermets 50WC-50Cu$_{cycle4}$ and 25WC-75Cu$_{cycle2}$, the increase in content of copper did not cause a significant increase in the thermal diffusivity of the cermets. Notice that the densification for both materials is similar.

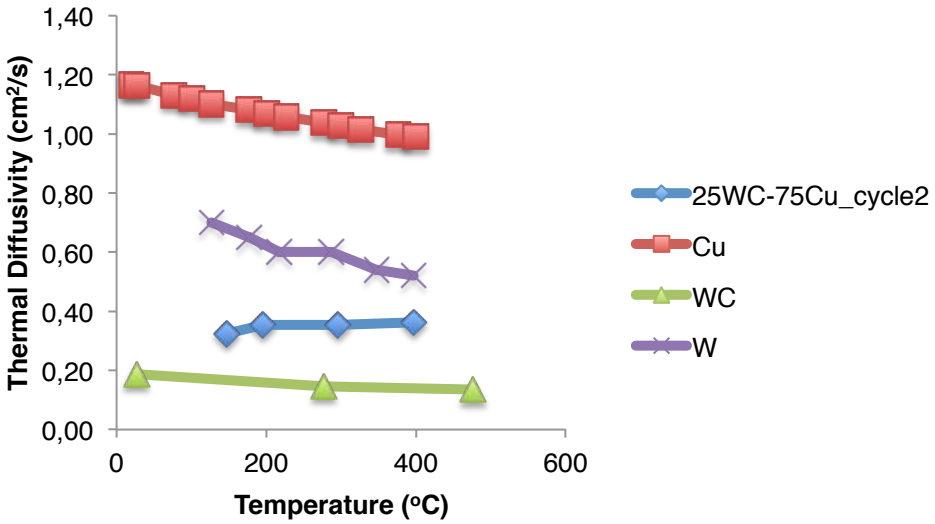

Figure 3.23: Thermal diffusivity as function of temperature of the 25WC-75Cu$_{cycle2}$ cermet.

3.4 References

[1] "PURE COPPER." [Online]. Available: http://www-ferp.ucsd.edu/LIB/PROPS/PANOS/cu.html. [Accessed: 21-Jul-2015].

[2] R. M. German, *Liquid Phase Sintering*, First. Plenum Press New York, 1985.

[3] W. D. Schubert, a. Bock, and B. Lux, "General aspects and limits of conventional ultrafine WC powder manufacture and hard metal production," *Int. J. Refract. Met. Hard Mater.*, vol. 13, no. 5, pp. 281–296, 1995.

[4] E. Hong, B. Kaplin, T. You, M. S. Suh, Y. S. Kim, and H. Choe, "Tribological properties of copper alloy-based composites reinforced with tungsten carbide particles," *Wear*, vol. 270, no. 9–10, pp. 591–597, 2011.

[5] a. R. Kennedy, J. D. Wood, and B. M. Weager, "Wetting and spontaneous infiltration of ceramics by molten copper," *J. Mater. Sci.*, vol. 35, no. 12, pp. 2909–2912, 2000.

[6] O. J. Kwon and D. N. Yoon, "Closure of Isolated Pores in Liquid Phase Sintering of W-Ni," *Inter. J. Powder Met. Powder Tech.*, vol. 17, pp. 127–133, 1981.

[7] M. HUMENIK and N. M. PARIKH, "Cermets: I, Fundamental Concepts Related to Micro-structure and Physical Properties of Cermet Systems," *J. Am. Ceram. Soc.*, vol. 39, no. 2, pp. 60–63, 1956.

[8] N. M. Parikh and M. Humenik, "Cermets: II, Wettability and Microstructure Studies in Liquid-Phase Sintering," *J. Am. Ceram. Soc.*, vol. 40, no. 9, pp. 315–320, 1957.

[9] W. D. Kingery, J. M. Woulbroun, and F. R. Charvat, "Effects of applied pressure on densification during sintering in the presence of liquid phase," *J. Am. Ceram. Soc.*, vol. 46, no. 8, pp. 391–395, 1963.

[10] F. J. Paneto, J. L. Pereira, J. O. Lima, E. J. Jesus, L. a. Silva, E. Sousa Lima, R. F. Cabral, and C. Santos, "Effect of porosity on hardness of Al2O3–Y3Al5O12 ceramic composite," *Int. J. Refract. Met. Hard Mater.*, vol. 48, pp. 365–368, 2015.

[11] M. Fujitsuka, B. Tsuchiya, I. Mutoh, T. Tanabe, and T. Shikama, "Effect of neutron irradiation on thermal diffusivity of tungsten- rhenium alloys," *J. Nucl. Mater.*, vol. 287, pp. 1148–1151, 2000.

[12] M. Akoshima, Y. Yamashita, Y. Hishinuma, T. Tanaka, and T. Muroga, "Thermal Diffusivity Measurements of Candidate Ceramic Materials for Shielding Blankets," in *ECTP2014 - 20th European Conference on Thermophysical Properties*, 2014.

[13] K. M. Zwilsky and E. L. Langer, *ASM Handbook Volume 3: Alloy Phase Diagrams*, vol. 3, no. 3. ASM International, 1982.

[14] M. Jeandin, Y. Bienvenu, and J. L. Koutny, "Liquid Phase Sintering of Nickel Base

Superalloys," *Superalloys 1984 (Fifth Int. Symp.*, pp. 467–476, 1984.

[15] Y. V. Naidich, I. A. Lavrinenko, and V. A. Evdokimov, "Densification in liquid phase sintering under pressure in the system tungsten-copper," *Sov. Powder Metall. Met. Ceram.*, vol. 13, no. 1, pp. 26–30, 1974.

[16] M. Kumazawa, "Mechanism of crystal growth and coalescence of tungsten carbide in the presence of cobalt liquid phase," *Mater. Trans.*, vol. 31, no. 8, pp. 685–688, 1990.

[17] W. Xu, "Grain growth, densification and mechanical properties of nanocrystalline WC-Co," The University of Utah, 2008.

[18] R. L. Coble and T. K. Gupta, "Intermediate Stage Sintering," in *Sintering and Related Phenomena*, G. C. Kuczynski, Ed. New York: Gordon and Breach, 1967, p. 423.

[19] "Accuracy, Precision and Detection Limits | MyScope." [Online]. Available: http://www.ammrf.org.au/myscope/analysis/eds/accuracy/. [Accessed: 20-Oct-2015].

[20] F. Elfallagh and B. J. Inkson, "3D analysis of crack morphologies in silicate glass using FIB tomography," *J. Eur. Ceram. Soc.*, vol. 29, pp. 47–52, 2009.

[21] R. Warren, *Ceramic Matrix Composites*. Blackie and Son, Ltd, 1992.

4 Conclusions and Future Work

WC-Cu cermets containing 25, 50 and 75 vol. % of copper were produced via liquid phase sintering by hot pressing. The optimization of the consolidation parameters showed that as the WC content of material increases the pressure required to achieve high densification increases as well. To achieve high densifications a compromise between temperature and pressure applied during hot pressing must be established.

Densifications above 90% were achieved for all the three compositions. The highest pair of pressure and temperature (1100ºC and 47 MPa) was applied to the 75WC-25Cu cermets in order to compact the ceramic phase and force the small amount of liquid copper to fill the pores, achieving this way the higher densification (95%). Densification of the 25WC-75Cu samples were difficult to achieved due to the high content of copper that escapes the mold when high pressures (above 22 MPa) were applied.

The formation of liquid copper was observed in all samples consolidated even at temperatures bellow the melting temperature of copper. The formation of liquid phase is associated to the presence of impurities and to the error of the pyrometer.

Coalescence of particles was observed in cermets with high WC content (50 and 75 vol. %). The formation of copper islands is reduced by larger mixing times in turbula, which promotes a better homogenization of the final microstructure of the cermets. However, in the 75WC-25Cu cermets some copper islands were found due to the high pressure applied that forced the liquid copper to fill the pores during sintering.

The results show that Vickers hardness (HV0.2) of the cermets increased with increasing WC content. The particles showed a good adhesion with the copper matrix and no decohesion was observed for all samples.

Figure 4.1 shows the thermal diffusivity as function of the temperature of the denser materials produced for each composition. It can bee seen that the 75WC-25Cu cermets presents the lower diffusivity of the three cermet compositions tested due to it low copper content. The densities of the 50WC-50Cu and 25WC-75Cu are very close (92 and 91%, respectively) and despite the difference in copper content the thermal diffusivity of both materials is very close. This suggests that some microstructural features are responsible for such behavior. Other aspects may influence the thermal conductivity (and thermal diffusivity) of cermets such as porosity, impurities and thermal contact resistance at the particle/matrix interface and a more comprehensive study of these effects on the thermal diffusivity of WC-Cu cermets is required. The thermal diffusivity of the cermets produced using hot pressing consolidation with copper content varying from 25% to 75% is lower than pure Cu and WC indicating that these cermets are good candidates for thermal barriers.

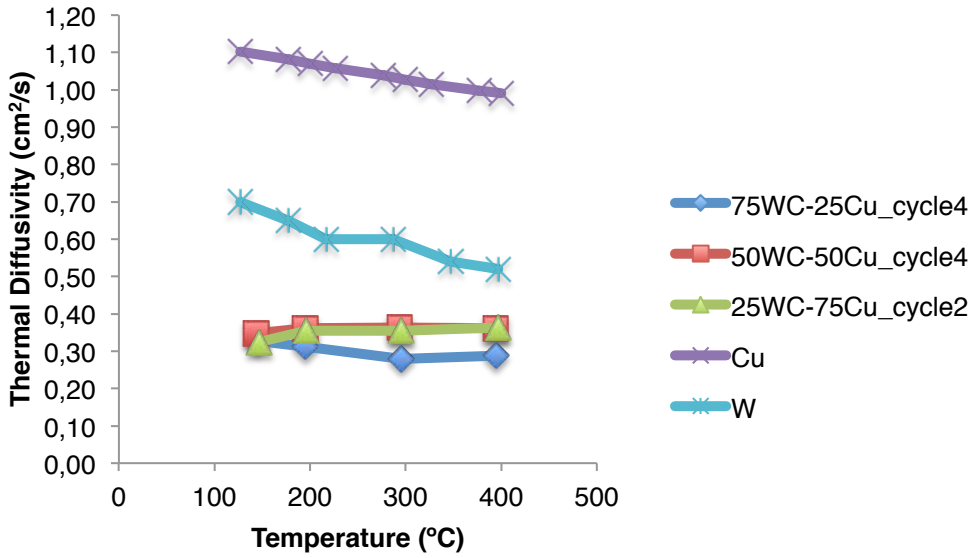

Figure 4.1: Thermal diffusivity as function of the temperature of the denser cermets for each composition.

Nevertheless, further characterization of the cermets is required to qualify these materials as thermal break interlayer candidates. Material's properties of interest would be Young's modulus which can be determined by tensile tests and coefficient of thermal expansion determined by a dilatometer.

The energetic neutrons (14 MeV) resulting for the fusion reaction inside the reactor can penetrate the plasma facing layer and achieve the thermal barrier. Therefore neutrons can be simulated using H^+ irradiation under appropriate ballistic conditions. It would be important to study the behavior of WC-Cu materials under H^+ irradiation using ion beam techniques.